The Potential of Spaceborne GNSS Reflectometry for Soil Moisture, Biomass, and Freeze–Thaw Monitoring

Summary of a European Space Agency-funded study

NAZZARENO PIERDICCA, DAVIDE COMITE, ADRIANO CAMPS, HUGO CARRENO-LUENGO, LUCA CENCI, MARIA PAOLA CLARIZIA, FABIANO COSTANTINI, LAURA DENTE, LEILA GUERRIERO, ANTONIO MOLLFULLEDA, SIMONETTA PALOSCIA, HYUK PARK, EMANUELE SANTI, MEHREZ ZRIBI, AND NICOLAS FLOURY

This work presents an overview of the activity developed in the frame of a project funded by the European Space Agency (ESA). The research was focused on the study of the potential applications of GNSS Reflectometry (GNSS-R) over land, with an emphasis on soil moisture (SM) and biomass. A study about the sensitivity with respect to the freeze–thaw dynamics was considered as well. The work started with an analysis of the sensitivity of GNSS-R reflectivity collected by the *TechDemoSat-1* (*TDS-1*) experimental satellite, although, to a limited extent, the Cyclone GNSS (CyGNSS) constellation was considered as well. The encouraging sensitivity outcomes led to the development of retrieval algorithms: three different approaches for SM and one for biomass based on neural networks.

A more theoretical investigation was carried out to better understand and predict the signal from a satellite platform, which required the updating of two different models. Topography effects and sensitivity to moisture and roughness of a rough soil were included as well as the effect of vegetation cover.

The project was carried out by a large team involving different research groups in Europe. It has led to main conclusions and recommendations derived from a beneficial collaboration and fertilization of ideas. The primary approaches and outcomes are summarized here, including comparisons to the recent literature.

Digital Object Identifier 10.1109/MGRS.2021.3115448
Date of current version: 9 November 2021

INTRODUCTION AND STATE OF THE ART OF GNSS-R

GNSS-R is a technique that exploits the signals of opportunity provided by navigation satellites to implement a multistatic radar system for remotely sensing different biogeophysical parameters [1]–[3]. This can be achieved by means of receivers looking downward, cross-correlating the reflected signal either with a replica of the transmitted one (i.e., conventional GNSS-R) or with the direct signal itself (i.e., interferometric GNSS-R). The received signal power is delivered as a function of the time delay (sampled according to the GNSS signal bandwidth) and Doppler frequency due to the motion of the platform and Earth (sampled according to the coherent integration time); the resulting delay-Doppler map (DDM) represents the main observable. Recent experiments have been carried out from airborne platforms but also from satellites (e.g., the UK-Disaster Monitoring Constellation, *TDS-1*, and Federated Satellite Systems on 3Cat). A NASA mission, the CyGNSS [4], collecting reflections from a constellation of eight small platforms, is currently operating to monitor tropical cyclones and study ocean winds.

In the last decade, the ESA has stimulated the growth of this technology, funding ground-based and airborne experiments and even designing spaceborne receivers to perform altimetry of the ocean surface, i.e., the Passive Reflectometry and Interferometry System In-orbit Demonstration and the GNSS-R Radio Occultation and Scatterometry onboard the International Space Station (GEROS-ISS) mission [5]–[7]. Based on this heritage, a research team has also proposed an ESA Earth Explorer based on this technique (the GNSS transpolar Earth reflectometry exploring system) [8]. Very recently, the HydroGNSS scout mission has also been established [9].

Recently, the ESA has funded a research project that was run by a large European team with consolidated experience in GNSS-R modeling and data processing for land applications [6], [10]–[19]. The project aimed at demonstrating 1) to what extent the current knowledge from models and past ground/airborne experiments on GNSS-R applications for SM and vegetation biomass retrieval is still applicable from space (including a preliminary analysis on the monitoring of the freeze–thaw state), 2) which additional phenomena should be modeled and/or explained, and 3) which final biogeophysical products are possible to deliver and how (with recommendations for future systems). We mention that even if the project and, therefore, this manuscript only focus on the retrieval of SM, biomass, and freeze–thaw state, other very important land parameters can be monitored and characterized by means of GNSS-R. Some of these are floods [20]–[23], wetland states and dynamics [24], and land/ice altimetry [16], [25], [26]. We just note that SM retrieval is quite mature and largely investigated, whereas, for biomass and freeze/thaw, the project was more explorative in view of future missions. All of these variables play an important role in studying and understanding the carbon and energy cycle of Earth and the monitoring of the environment.

The project has stimulated very beneficial discussions and a cross-fertilization of ideas. Many articles have already been published by individual research groups taking part in the project, but the relevant tasks and main achievements will be outlined throughout this article. This can contribute to providing a comprehensive summary of the final responses to the addressed scientific questions. Besides the details that can be found in the referenced literature, this article offers a comparative summary of the results achieved by the different teams and synthesizes the project conclusions about the potential and drawbacks of GNSS-R applications over land. This is also done with comparisons to the recent literature.

A review of the state of the art was carried out at the beginning of the project, followed by the collection, quality control, and detailed analysis of experimental GNSS-R data over land, with a strong focus on the spaceborne data sets provided by the TDS-1 mission [27] and, although to a limited extent, by the

CyGNSS mission [4]. As a by-product, the TDS-1 Level 1 (L1) b data collected during the full mission lifetime were organized and preprocessed to create a manageable set of files (one for each year on a global scale and one for each test site along the full mission lifetime).

The main scope was the investigation of the sensitivity of the data to the target land parameters and the effects of additional biogeophysical parameters on the GNSS-R observations. Some data collected by the airborne GLObal navigation satellite system Reflectometry Instrument (GLORI) sensor [12], [17] in France and the Compact Reflectometer for Terrain Observations (CORTO) sensor [18] in Spain were also analyzed and compared to the spaceborne data to understand to what extent the platform height can affect both sensitivity and retrieval capability. Another promising application of GNSS-R over land that was investigated is the monitoring of freeze–thaw soil conditions in subarctic areas [28], which has attracted scientific interest from different groups [29]–[32].

THE ESA HAS FUNDED A RESEARCH PROJECT THAT WAS RUN BY A LARGE EUROPEAN TEAM WITH CONSOLIDATED EXPERIENCE IN GNSS-R MODELING AND DATA PROCESSING FOR LAND APPLICATIONS.

Different approaches to retrieve SM, above-ground forest biomass (AGB), and tree height or vegetation optical depth (VOD) from *TDS-1* and CyGNSS data were developed and tested [33]–[37]. Vegetation parameters were even retrieved from the ground by placing the receiver under vegetation [11], [38].

Changes in the *TDS-1*-received power were consistently associated to changes in SM, with a dynamic in the order of 7 dB, even though soil roughness and vegetation were recognized as having an impact. Changes in CyGNSS-reflected power were also found to be linearly correlated to changes of Soil Moisture Active Passive (SMAP) products [35]. In the presence of low vegetation, the sensitivity of the *TDS-1* signal-to-noise ratio (SNR) to SM measured by the *Soil Moisture and Ocean Salinity* (*SMOS*) satellite was found globally to be in the order of 8 dB/(m^3/m^3) in [34].

In [41], it is demonstrated that the CyGNSS constellation is able to improve sampling the SM product from the SMAP mission onto a 36-km grid. The combined near-operational SM product is noisier than SMAP's but achieves a highly appreciable temporal sampling of 6 h.

Algorithms to retrieve SM from CyGNSS data only (i.e., independently of SMAP or SMOS products) have been proposed using artificial neural networks (ANNs) [42], [43]. They can include as input other quantities affecting the GNSS-R signal [e.g., the normalized difference vegetation index (NDVI)], introduce additional observables (e.g., derived from the full DDM), and take into account the nonlinearity of the relationships among inputs and the SM output. In [43], an ANN regressor was trained and tested using an in situ SM from the International Soil Moisture Network (ISMN), and subdaily retrievals over a 9-km × 9-km cell achieved a root-mean-square error (RMSE) of 0.054 m^3/m^3. Similarly, in [42], an improvement of the retrieval performances was also found when increasing the integration time; a comparable accuracy of CyGNSS and SMAP products when both were compared to ISMN data was observed as well.

A simple forward model was proposed in [44], leveraging on the microwave radiometry heritage. Although the GNSS-R signal is recognized as a mixture of coherent and incoherent scattering, an equivalent reflectivity is considered as the main observable. The model accounts for the influence of surface reflection, the vegetation attenuation, and volume scattering, and a few model parameters were tuned using a matchup of CyGNSS and SMAP data. The model was conceived as first step for future model-based inversion.

A different approach was proposed in [45], based on the assumption that, on a short time scale, the SM can produce changes in the CyGNSS bistatic normalized scattering coefficients, whereas soil roughness and vegetation do not change much. Note that in [45] only incoherent scattering was selected, in contrast to other articles, where a coherent reflection from the land surface was assumed. The change detection approach is able to estimate only changes in SM, so prior statistics from SMAP were needed to deliver absolute values. The SM maps on a 0.2° × 0.2° grid and a one- or three-day temporal sampling were compared to the SMAP data, and the RMSE was found to be in the order of 0.03–0.04 m^3/m^3.

The progress in vegetation parameters and freeze–thaw state from spaceborne GNSS-R sensors is less mature. The GNSS-R signatures of different land-cover (LC) types (forest, ice, and so on) were analyzed empirically using GNSS reflections collected by the SMAP radar receiver, taking advantage of the dual linearly polarized antenna and its high gain [46]. Specifically, the sensitivity of the soil reflection to the attenuation of vegetation in a near-specular geometry was previously addressed, with a theoretical approach, in [14]. This was empirically verified using reflectivity and a zero-Doppler waveform trailing edge derived from the CyGNSS DDMs. Regarding the freeze–thaw state, the expected change in reflectivity modeled according to the SMAP freeze/thaw was actually observed in the GNSS-R scenario captured by the SMAP radar receiver [32].

In this project, three different approaches were tested for SM: a physically based algorithm applied to a single satellite passage, an empirical multilinear regression approach, and a change detection approach based on a multitemporal data stack. The physical approach was tested on airborne and satellite *TDS-1* data, concentrating on understanding how to collect the needed ancillary information, which was revealed to be a major problem. The multilinear regression and change detection approaches have been applied to data resampled on a regular grid and averaged over time (e.g., to retrieve daily means). The former was applied on a global as

well as a local scale, the availability of ancillary data being different for the two cases. The latter can retrieve a saturation index to be successively converted into volumetric SM. Retrieval approaches based on ANNs were also attempted for different target parameters (biomass, tree height, VOD, and SM), whose reference values (the training and test sets) were provided by different sources. In detail, the ANN algorithms were employed to retrieve the forest biomass and the tree height at a global scale from CyGNSS data and to provide daily estimates of SM and VOD [47].

An additional study carried out in the project framework dealt with the modeling of the reflected GNSS signal over land observed from space, merging the experiences of two research groups. The two software tools developed in the past by the two different teams have been updated to improve the modeling accuracy and include specific satellite-related effects. The GEROS-ISS end-to-end simulator [48] has been updated for predicting the land signal, introducing a simple first-order solution for vegetation attenuation/scattering (see [49]). The Soil and Vegetation Reflection Simulator (SAVERS) [50] has been updated (see [51]) and used to understand the contribution of near-specular and diffuse incoherent signals at spaceborne height, implementing the model described in [52]. Both tools account for surface topography and target inhomogeneity, whose effects on the satellite signal have been recognized and discussed. The simulators were used to derive the theoretical sensitivity of the signal to the surface parameters, to be compared with that observed on the data [19], [51].

This article is a summary of the project's final report [53], attempting to establish the work on the state of the art of the GNSS-R technique.

DATA SET DESCRIPTION AND CALIBRATION

The work was carried out by exploiting the data from two spaceborne platforms: *TDS-1* and CyGNSS. *TDS-1* L1b products in NetCDF format were collected from the Measurement of Earth's Reflected Radio-Navigation Signals by Satellite (MERRBYS) portal [54]. The original data are split into 6-h segments. To facilitate the scientific exploitation of the data, they have been arranged in a single file over a period of time: one year for the global database and the whole mission lifetime for specific test sites. The processed data contain the most significant set of variables for the analysis and investigation of biomass and SM sensitivity. CyGNSS L1 data [55], version 2.0 (the one available at the time of the work), were collected from the Physical Oceanography Distributed Active Archive Center ftp server [56].

The main observable extracted from both products is the DDM power, which must be converted into a calibrated observable using ancillary information included within the files. Namely, the peak SNR and the reflectivity were computed. The latter has been derived assuming the signal is dominated by the coherent component of the surface scattering in the near-specular direction, so that the power received by the down-looking antenna (P_{rp}^{S}), starting from the well-known radar equation for deterministic targets (see, e.g., [57]), can be written as follows:

$$P_{rp}^{S} = \Gamma_{pq}(\theta)\frac{\lambda^2 G^t G^r P_t}{(4\pi)^2 (R_r + R_t)^2}, \tag{1}$$

where R_r is the distance from the receiver to the specular point (SP), R_t is the distance from the transmitter to the SP, λ is the wavelength, and G^t and G^r are the gain of the transmitting and receiving (i.e., down-looking) antennas. Γ_{pq} is the surface (equivalent) reflectivity, which is a function of the incidence angle θ at the SP, for transmitted q polarization (right-hand circular polarization for GPS systems) and received p polarization [left-hand circular polarization (LHCP) as for *TDS-1* and CyGNSS]. To retrieve the unknown transmitter equivalent isotropic radiated power, i.e., $EIRP = G^t P_t$, the amplitude of the direct signal collected by the *TDS-1* up-looking antenna was exploited as described in [58]. As for CyGNSS, the EIRP was retrieved from the L1 product itself. Both approaches have serious drawbacks: for example, the up-looking antenna pattern is not accurately known, whereas the nominal values of the EIRP can be inaccurate. Additionally, the power of the noise must be estimated from the DDM using the first delay lines preceding the peak; this is then subtracted from the received power to retrieve the signal power.

The equivalent reflectivity embeds the effects of the surface moisture content, small-scale roughness, and the attenuation introduced by the vegetation cover. Such an observable is denoted the *equivalent reflectivity* as it also includes the contribution of the incoherent component of the scattered field introduced by the vegetation and soil roughness at different scales. In this respect, we mention that, during the development of the project, different research groups have deeply investigated the phenomenology of GNSS-R land scattering, considering both theoretical and experimental approaches (see [16], [26], [59], and [60] and the references therein). In this frame, the need of modeling the presence of an intermediate scale of roughness and accounting for the incoherent nature of the scattering for most of the observed land surfaces (excluding water bodies, iced surfaces, and almost-planar surfaces characterized by large values of the correlation length) has been discussed. The relative weight of coherent and incoherent signals in the GNSS-R data is probably still a main research question (as well as how to distinguish between the two).

In the analysis presented in the sequel, a quality filtering of the *TDS-1* data was applied to remove cases with the spacecraft in eclipse or with the direct signal potentially entering the DDM. In most cases, only small incidence angles (e.g., less than 45°) were considered, as signals at larger angles are collected far from the boresight of the down-looking antenna, which can introduce calibration problems caused by a poor knowledge of the attitude. Data collected over complex

topography were also removed from the analysis. We also removed CyGNSS data with poor quality flags and those collected over continental surfaces with altitudes greater than 500 m since the small receiving window was initially set to collect data from the ocean and probably cannot accommodate data coming from high mountains. Note that, after December 2017, reflections coming from altitudes greater than 500 m could be successfully collected by CyGNSS.

THE EQUIVALENT REFLECTIVITY EMBEDS THE EFFECTS OF THE SURFACE MOISTURE CONTENT, SMALL-SCALE ROUGHNESS, AND THE ATTENUATION INTRODUCED BY THE VEGETATION COVER.

The research on the retrieval of soil and forest parameters needs reference global information, such as SM, biomass, and tree height or VOD for carrying out correlation analyses and validating the relevant retrieval algorithms. SM and VOD were obtained from microwave radiometer products, i.e., the SMAP L3 daily products, version 5, projected onto the Equal-Area Scalable Earth (EASE)-Grid, and the SMOS L3 product.

Note that the VOD is not a vegetation parameter that can be measured on the ground; it is, rather, an electromagnetic parameter that is correlated with the vegetation biomass and height. Moderate-Resolution Imaging Spectroradiometer/Terra NDVIs generated every 16 days were also collected. For forests, the Ice, Cloud, and Land Elevation Satellite (ICE)-Geoscience Laser Altimeter System (GLAS) lidar acquisitions processed as in [61] were considered to provide tree height maps as well as the improved pantropical AGB [62], limited to +/- 40° of latitude (available from www.wageningenur.nl/grsbiomass). The time intervals used for colocating different products were rather short for the estimates of SM (2–3 h) but were more relaxed for biomass estimates as the reference data can be considered mainly "static" maps that do not provide any evolution in time.

The sensitivity analysis and the retrieval were carried out on both a global and a local scale (i.e., over specific test areas). The latter were selected with different criteria, with the aim of covering different soil and forest conditions and getting a suitable amount of ancillary data. Specifically, for SM, the following locations were considered: Florida, Texas, the SMOSMANIA (France), the Merguellil site (Tunisia), the REMEDHUS site (Spain), and the CEMADEN site (Brazil). For biomass, the selected areas were Alaska, Florida, Manaus, Argentina, Zambia, and Finland. Additional areas to test the effect of topography were Chad and the Alps.

The study related to the GNSS-R potentiality for freeze/thaw monitoring was carried out in the Northern Hemisphere. An analysis aimed at comparing SMAP freeze/thaw and GNSS-R spatiotemporal dynamics was performed in Siberia. Comparisons between GNSS-R data and in situ temperature records were accomplished by taking advantage of stations located in Canada, Finland, Siberia, and Alaska.

SENSITIVITY TO SM

ANALYSIS OF TDS-1 *DATA*

The sensitivity of *TDS-1* observables to the surface SM was investigated using the 2014–2017 global TDS-1 data set. The sensitivity of different GNSS-R observables to the surface SM and its dependence on the incidence angle were analyzed. A global scale statistical analysis using SMOS L3 products (SMOS nominal resolution, regridded at 25 km) was first carried out. Then, an investigation at regional scale using SMOS L4 products (1-km resolution) as well as in situ sensors was performed. The potential dependence on the subsurface SM was also analyzed in the Brazilian semiarid region using the LISFLOOD [63] and MUSA models (http://musa.cptec.inpe.br).

The *TDS-1* reflectivity was first corrected to compensate for the vegetation effects using the SMOS-derived VOD. A simple model is assumed considering the vegetation two-way attenuation and the small-scale surface roughness *HR* parameter used in the SMAP retrieval algorithm, as given in the following:

$$\Gamma(\theta_i, \mathrm{SM}, \mathrm{VOD}) = \Gamma(\theta_i, \mathrm{SM}) \cdot e^{-HR} \cdot e^{-2 \cdot \mathrm{VOD}/\cos(\theta_i)}. \quad (2)$$

It must be pointed out that mixed-pixel effects were not accounted for, and the resolution of SMOS products (35–50 km) is significantly different from that of GNSS-R products as the latter can be approximately determined by the size of the first Fresnel zone in the case of coherent scattering [52], [59], [66]–[68] or as about 25 km as a maximum for incoherent scattering. The relatively low correlation of the results shown in Figures 1 and 2 may be partially attributed to the different resolution of the measurements, which was not considered (about 1–10 km for TDS) when incorporating the SMOS and SMAP data (i.e., VOD and *HR*) into (2).

Figure 1 shows the scatterplots of SNR, DDM peak, and reflectivity (compensated for vegetation and the distance factor and limited to incidence angles up to 30°) versus the colocated SMOS L3 SM product. The color scale shows the VOD in nepers. Note that the pixels with the highest VOD are well above the fitting line, which suggests that the VOD effects must be considered, but that the correction in (2) is overcompensating for these effects.

As can be seen, the SNR exhibits the largest uncertainty (standard deviation $\sigma = 7.1$ dB) but also the largest sensitivity to SM, i.e., 22.75 dB/(m^3/m^3). The peak of the DDM exhibits a very weak sensitivity to SM, as the signal is masked by the speckle noise. The reflectivity scatterplot exhibits a sensitivity to SM of 9.11 dB/(m^3/m^3) and a much smaller uncertainty of $\sigma = 3.17$ dB. From now on, only the reflectivity will be analyzed [19].

Figure 2 shows the scatterplots of the (calibrated) reflectivity for incidence angles from 0° to 30° [Figure 2(a)], from 30° to 60° [Figure 2(b)], and from 60° to 90° [Figure 2(c)] versus the colocated SMOS SM. One can see that, as the incidence angle increases, the sensitivity to SM decreases: 8.7 dB/(m^3/m^3) from 0° to 30°, 5.7 dB/(m^3/m^3) from 30° to 60°, and 2.8 dB/(m^3/m^3) from 60° to 90°, while the pixels more affected by dense vegetation (i.e., large VOD) depart more from the linear fit.

While the obtained sensitivities are lower than those obtained in previous studies mentioned in the introduction (see [34] and [38]), they are still significant. Note that any speculation about the presence of speckle noise refers back to the question about the relative weight of coherent and incoherent scattering, which is the object of studies in the recent literature as discussed previously [16], [45].

A similar analysis was also performed over three different regions where a 1-km-resolution L4 downscaled SMOS surface SM was produced and in situ data were available. L4 SM maps were obtained from the L3 SM maps by applying a downscaling algorithm to disaggregate the original SM pixels to a 1-km resolution [69], [70].

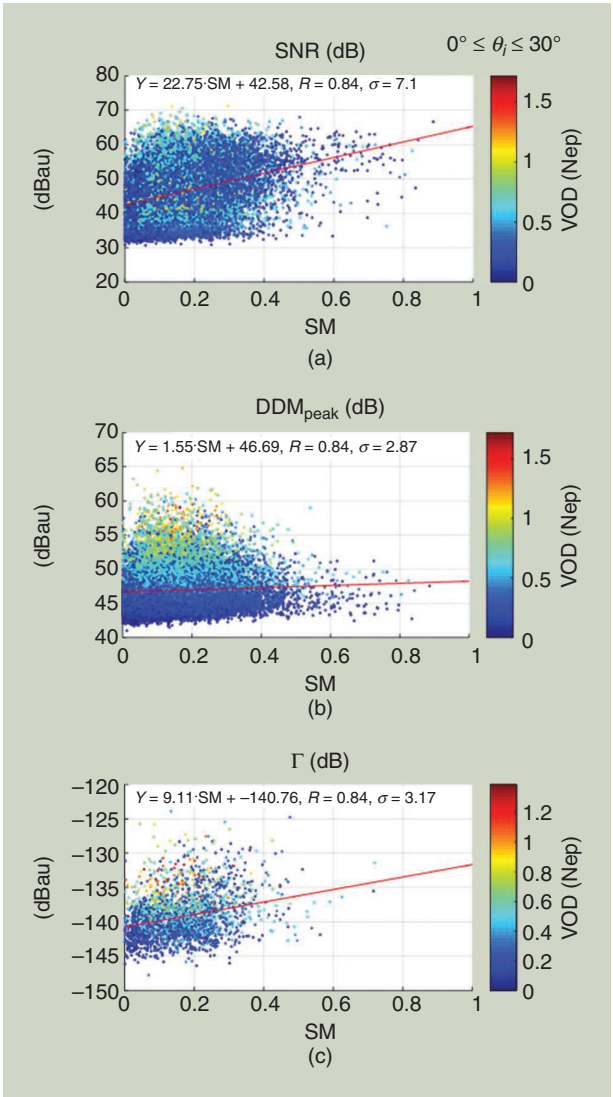

FIGURE 1. Screened and compensated *TDS-1* GNSS-R observables versus *SMOS* SM data. The color scale represents VOD. (Source: [18].)

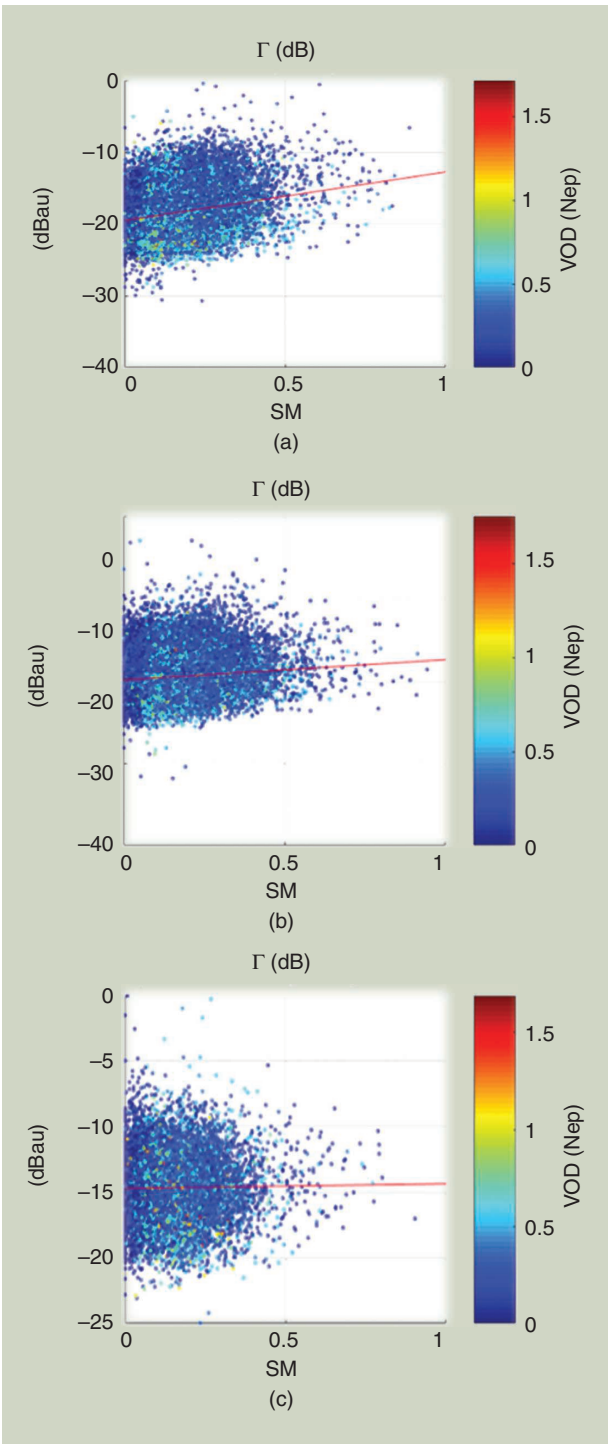

FIGURE 2. Calibrated *TDS-1* GNSS-R reflectivity (dB) at LRCP polarization versus SMOS SM data for different ranges of incidence angle: (a) from 0° to 30°, (b) from 30° to 60°, and (c) from 60° to 90°. (Source: [18].)

The considered regions were the CEMADEN area located in a Brazilian semiarid region, the REMEDHUS site in Spain, and the OzNet site in Yanco, Australia. These regions belong to SM networks. For the Brazilian site, hydrological models were run to estimate the 50-cm and 100-cm SM.

The *TDS-1* reflectivity was compared with SMOS L3 and L4 products, as well as in situ data from the ground networks. In principle, many colocated data should be available for intercomparison. In practice, *TDS-1* ground tracks are so far away from the network stations that few matchups were available, and only when the distance threshold is increased up to 30 km, the matchup samples become statistically significant. Unfortunately, this distance is similar to the *SMOS* L3 resolution, so that no conclusive results can be derived about the comparison at higher resolutions.

The sensitivities obtained using the SMOS L3 SM values can be considered quite high: 18.64 dB/(m^3/m^3) in Yanco, New South Wales (NSW), Australia; 9.37 dB/(m^3/m^3) in the CEMADEN area, Brazil; and 12.15 dB/(m^3/m^3) over the Iberian Peninsula. However, the sensitivity derived when compared to the SMOS L4 SM values decreased notably to 11.18 dB/(m^3/m^3) in Yanco, NSW, Australia; 6.62 dB/(m^3/m^3) in CEMADEN, Brazil; and –1.1 dB/(m^3/m^3) in the Iberian Peninsula (this is probably less significant because of the limited amount of data and the limited range of SM values). As the topography and/or vegetation effects increase, this sensitivity decreases, although the pixels affected by topography were flagged and discarded, and vegetation effects were, in principle, compensated for. In any case, all of these sensitivities are smaller than those obtained in [34] and [38], which are about 38 dB/(m^3/m^3). The nonlinearity of reflectivity versus SM values mainly explains this discrepancy. It is likely that certain experiments show a higher sensitivity since they explore low values of SM with respect to the present analysis, which regarded almost the full range of SM values. An investigation about this issue was done in the radar context in [71].

When trying to correlate the *TDS-1* GNSS-R reflectivity with in situ SM values, very few matchups were found. It was difficult to perform a robust fit over the REMEDHUS (Spain) and Yanco (NSW, Australia) sites. Only over Brazil, with a radius setting of 30 km, satisfactory matchups were found to obtain representative results. The sensitivities are equal to 7.39 dB/100%, 1.36 dB/(m^3m^3), and –9.10 dB/(m^3m^3) for incidence angles from 0° to 30°, from 30° to 60°, and from 60° to 90°, respectively. For incidence angles from 0° to 30°, the value obtained is between 6.62 dB/(m^3m^3) and 9.37 dB/(m^3m^3) evaluated with respect to L4 and L3 SMOS SM data, respectively. Because of the availability of the outputs of hydrological models (LISFLOOD and MUSA) in the Brazilian semiarid site, a comparison of reflectivity with SM in the root zone was attempted [19]. The results were not conclusive, again because of the small number of matchups. However, a sensitivity of the reflectivity to the SM at a 50-cm depth was observed using the LISFLOOD model (at 10-km resolution), whereas no apparent sensitivity to the 1-m depth SM from the MUSA model was observed, the latter running at a worse resolution (i.e., 25 km).

The problems encountered when analyzing the sensitivity at high resolution recalled another research question, which is the spatial resolution of the GNSS-R observations [66], which is related again to the issue of coherence of the collected signal [16], [45]. Moreover, it must be pointed out that the GNSS-R observations along the tracks of the specular points are not repeated systematically over a predefined spatial grid, and thus the matchup with in situ data can be problematic.

SUPPORTING DATA SET: THE AIRBORNE GLORI CAMPAIGN

Data from the GLORI polarimetric receiver [12], [17] were used to understand to what extent the satellite height can affect the GNSS-R performances. Two classes of crops are considered according to their leaf area index (LAI) in the sensitivity analysis of GNSS-R observables to SM. The objective of this choice is limiting the influence of the heterogeneity of vegetation cover densities between agricultural reference fields. The first class is defined by LAI 1, corresponding to medium and high vegetation densities. Figure 3 illustrates Γ_{RL} and the reflected SNR as a function of the SM, for the two LAI classes within the 0°–20° interval of incident angle. For each plotted point, the GNSS-R observables are averaged over an agricultural field at a given date. It can be seen that increasing the LAI generally reduces the sensitivity of GNSS-R observables to the SM.

The Γ_{RL} sensitivity to the SM decreases from 45.7 dB/(m^3/m^3) for the weak LAI values (LAI < 1) to 28.38 dB/(m^3/m^3) for the highest LAI values (LAI > 1). This result clearly illustrates the nuisance effect of the vegetation on GNSS-R observables. For the case of the polarimetric ratio (PR), defined as Γ_{RL}/Γ_{RR}, a low correlation with the SM was observed ($R^2 < 0.2$, even for low LAI values). For the low LAI class, a sensitivity slightly higher for both reflectivity and SNR for low incident angles was observed.

The GNSS-R observables were also studied as a function of the LAI of the plant cover. As in the case of SM, two incident angle intervals and three observables (Γ_{RL}, LHCP SNR, and PR) were considered. The effect of SM is reduced by considering data acquired in dry conditions, with the SM lower than 0.1 m^3/m^3. There is a clear decrease in the GNSS-R observables with increasing vegetation LAI because of the signal scattering and absorption (both increasing the optical thickness), as shown in Figure 4 [17]. The observed higher sensitivity to LAI at high incident angles (equal to –0.91 dB/[m^2/m^2]) can probably be attributed to a decrease in the influence of the soil component (roughness and moisture) due to an increment of the VOD.

A similar behavior is observed for the signal SNR. The PR observable was found to be correlated with the vegetation LAI, with a high sensitivity to vegetation LAI equal to –1.1 dB/[m^2/m^2] for high angles and –1.18 dB/[m^2/m^2] for low incident angles. This better performance of PR in comparison to its sensitivity to the SM could be explained by the highest effect of vegetation on the depolarization of the GNSS signal.

Based on the model in (2), and assuming an approximated linear dependence of the Fresnel reflectivity from SM and of VOD from the LAI, the equivalent reflectivity of a vegetated and rough soil in dB units can be written as follows:

$$\Gamma_{LR}(\theta)_{dB} = \alpha \cdot SM + \frac{\beta \cdot LAI}{\cos(\theta)} + \delta, \tag{3}$$

where α is the sensitivity of Fresnel reflectivity to the SM, β the sensitivity of canopy opacity to the vegetation LAI, and δ a constant related to the roughness effect. α, β, and δ are empirical parameters to be retrieved from the experimental data. The retrieved equation for the received left polarization is given in the following, where a linear relationship between the VOD and LAI is also applied:

$$\Gamma_{LR}(\theta)_{dB} = 40.73 \cdot SM - \frac{7.01 \cdot VOD}{\cos(\theta)} - 19.04. \tag{4}$$

Figure 5 presents a comparison between measured and simulated reflectivity over the training set (to retrieve the coefficients) and an independent validation set. As for the test set, the determination coefficient R^2 is 0.69, with an RMSE equal to 2.9 dB. Corn agricultural fields, with the highest vegetation height, are illustrated by the points showing the highest discrepancy and a saturation behavior

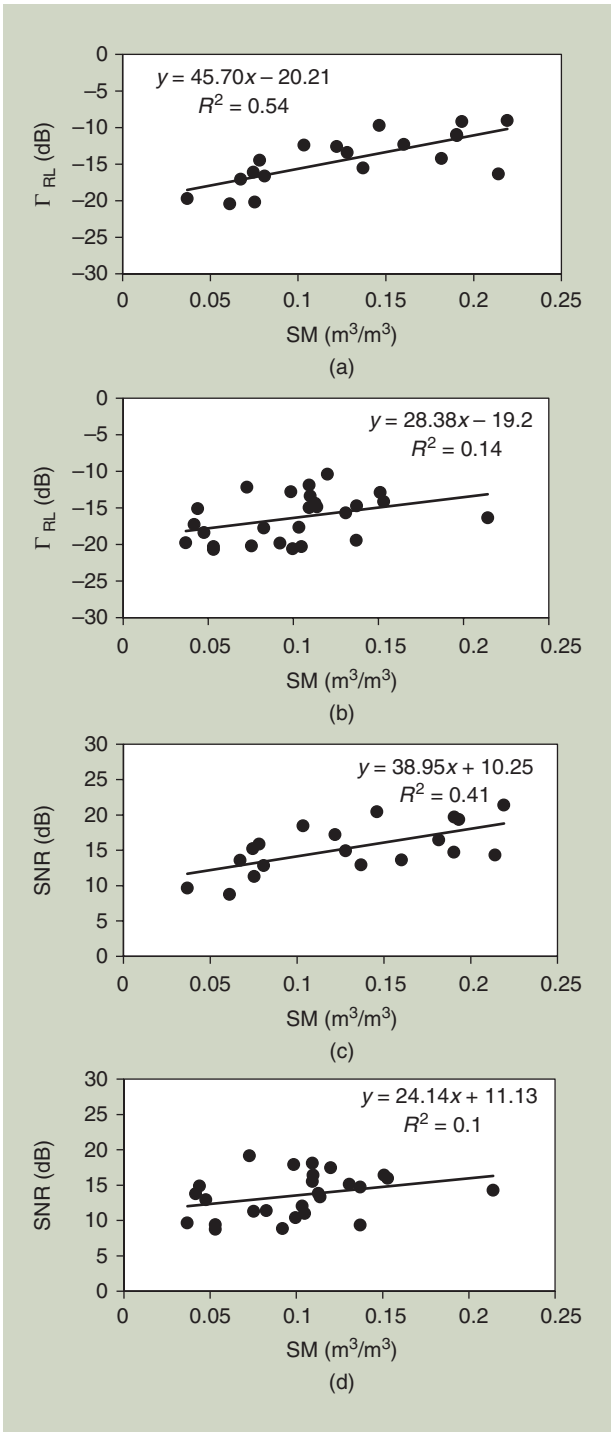

FIGURE 3. GNSS-R observables at 0°–20° incident angles as a function of SM: (a) Γ_{RL} for LAI < 1; (b) Γ_{RL} for LAI > 1; (c) SNR for LAI < 1; (d) SNR for LAI > 1. Data are relevant to the GLORI campaign; more information can be found in [17].

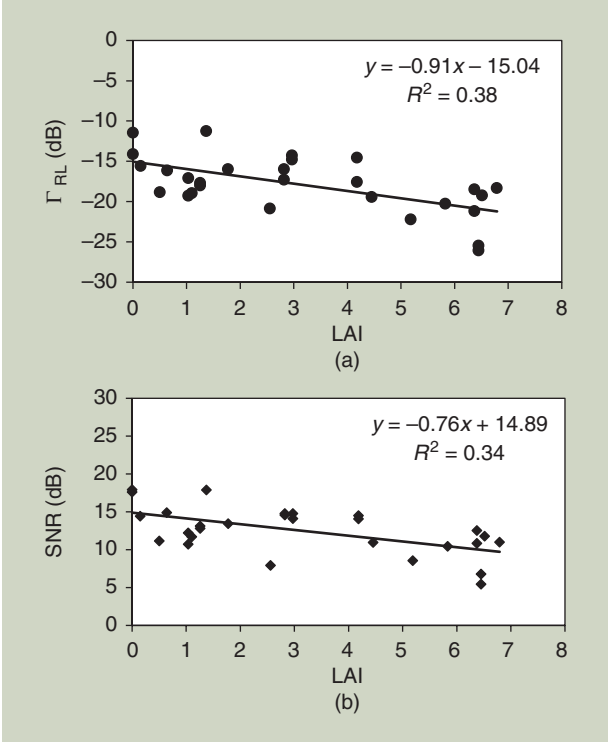

FIGURE 4. The GNSS-R observables at 20°–40° incident angles as a function of LAI at dry conditions (SM < 0.1 m^3/m^3): (a) Γ_{RL}; (b) SNR. (Source: [17].)

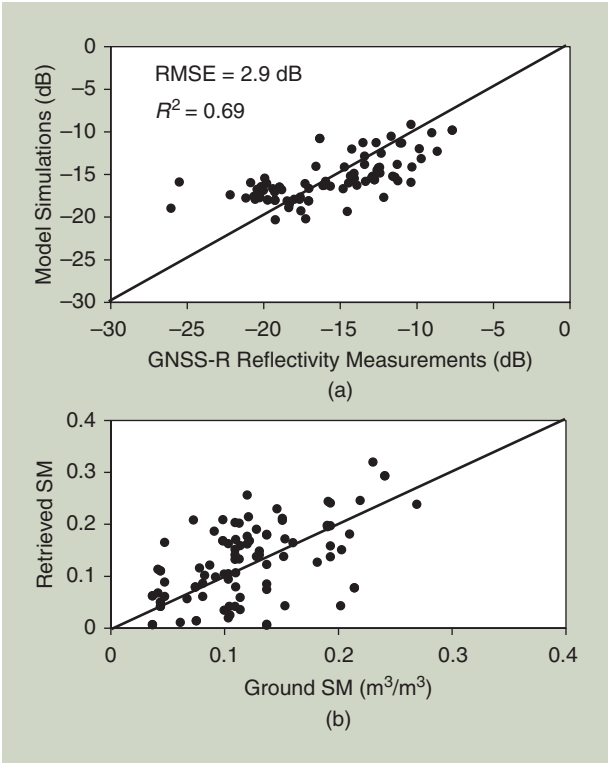

FIGURE 5. A comparison between retrieved reflectivity and ground measurements considering (a) the test set and (b) the validation set. The RMS difference for the retrieved SM is equal to 0.06 m^3/m^3. (Source: [17].)

for low values of reflectivity. The choice of the LAI as a proxy of optical thickness instead of other properties, such as the vegetation water content (VWC), could induce certain limitations.

Moreover, the sensitivity of the Fresnel coefficient to SM could be parameterized to the incidence angle, especially in the higher range of angles. Nonetheless, the simple model exhibits a fairly good capability to reproduce the data and can be adopted within a physically based retrieval approach. Of course, its validity for spaceborne data has to be verified.

THE SENSITIVITY OF CYGNSS DATA

As was done for *TDS-1*, the sensitivity of CyGNSS data to SM was assessed with respect to the SMAP SM. Note that reasonable results were obtained only by retaining SM data with the SMAP flag "retrieval recommended" (RR) set on. The sensitivity and its dependence on the incidence angle are shown in Figure 6. For small angles, the sensitivity appears relevant, even without compensating the effect of vegetation and roughness, and the data behavior appears similar to that of *TDS-1* data. Finally, the dependence of the CyGNSS reflectivity on vegetation has been analyzed in more detail using the VWC parameter, derived from NDVI climatology and included in the SMAP data (not shown here for the sake of conciseness). To provide an overall estimate of sensitivity to the SM and VOD, a multivariate regression analysis was carried out, as shown in Table 1. The

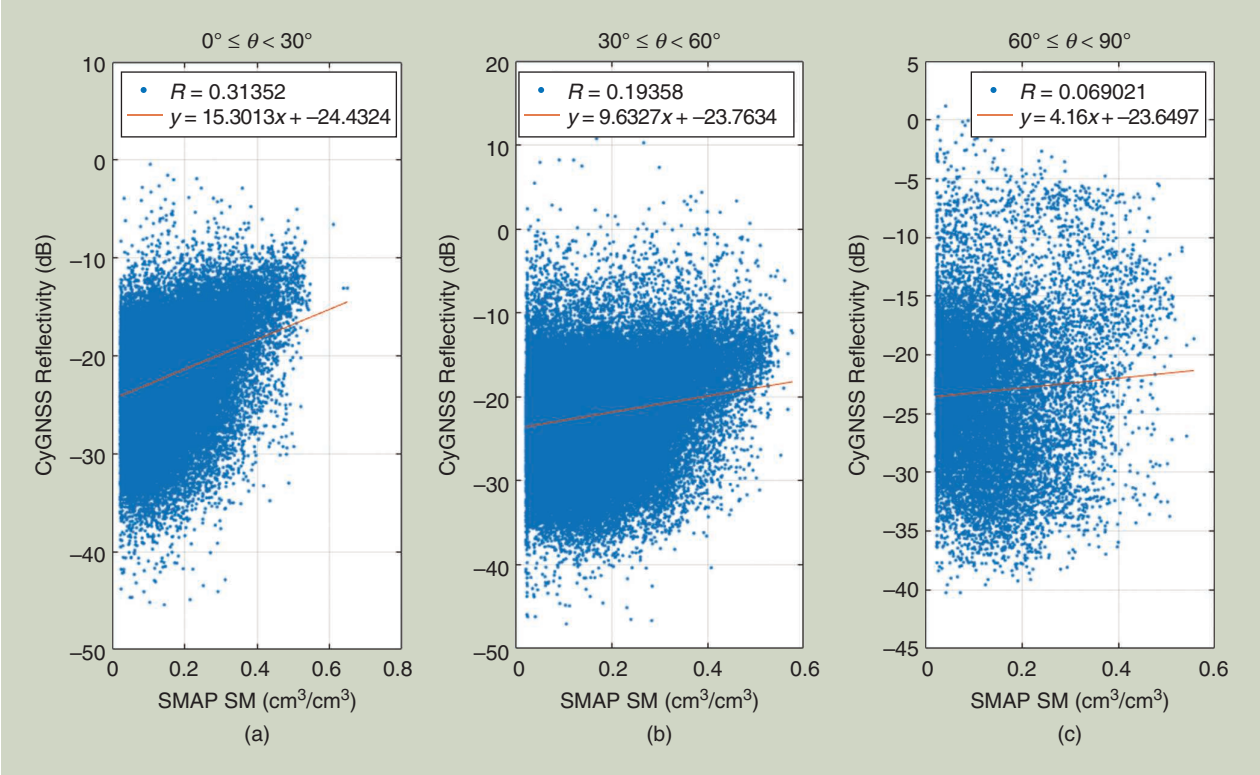

FIGURE 6. The dependence of sensitivity on the incidence angle, when the RR flag for SMAP data are applied: (a) from 0° to 30°, (b) from 30° to 60°, and (c) from 60° to 90°.

results show a good sensitivity to the SM and VOD (the latter being negative, as expected). The sensitivity to the SM is also quite independent of the incidence angle as the multivariate regression probably better compensates empirically for the VOD effect with respect to the physical model in (2). The sensitivity to the VOD is higher at larger angles, confirming previous outcomes.

SM RETRIEVAL APPROACHES

SINGLE-PASS RETRIEVAL

The feasibility to perform single-pass SM retrievals using GNSS-R observations and a physically based approach was investigated in [64] and [73]. The aim was to exploit data from a single receiver overpass, in contrast with the next sections, which discuss the retrieval of space and temporal means carried out based on empirical approaches. A single-pass approach does not need to resample and colocate observations over time; thus, it enables better temporal and spatial resolution. Another important advantage is the possibility of considering accurate forward models, describing the nonlinear relationship between reflectivity and SM, which exhibits a saturation effect for wet soils (see the previous discussion about the dependence of sensitivity on the SM dynamic range). The drawbacks are the need of an accurate absolute calibration and the collection of ancillary data to correct roughness and vegetation effects on each data sample.

The proposed physical SM retrieval algorithm exploits the model in (2) and inverts it to retrieve the Fresnel reflectivity using independent ancillary information on the VOD and roughness. The Fresnel reflection formula is used to derive the soil permittivity, and finally a permittivity model is exploited to retrieve the SM (among other variables, such as the clay fraction and physical temperature) through a minimization process.

The approach was first attempted on data acquired during an airborne experiment that took place on 22 October 2018 in an agricultural region around Balaguer, Catalonia, Spain. The plane was a Cessna Caravan flying at 1,200 m of height. The AISA instrument (a pushbroom hyperspectral sensor collecting 126 bands in the visible and near-infrared spectrum) flew together with the ARIEL L-band radiometer and the CORTO GNSS reflectometer at L1/L2 GPS bands [18].

The VOD used to compensate for the vegetation effects was derived following the SMAP approach [74] applied to the high-resolution NDVI available from AISA. A field campaign was carried out to collect data on surface roughness by a laser profiler and in situ SM measurements performed the same day as the airborne campaign. Ground samples were collected from five different areas corresponding to different agricultural fields. Surface roughness measurements were revealed to be quite critical, as usual, and the sampling was not dense enough. The ARIEL L-band radiometer [75] was used to provide a complete SM map with a final resolution of 0.8 m. The retrieved SM maps were then validated using the in situ SM samples.

Because of the limited estimation of the soil surface roughness from in situ data, the results show a disparity between the SM data retrieved by the ARIEL radiometer and the CORTO GNSS-R instrument. For a single track of reflections over a relatively flat area, the retrieved SM values are highly variable with the incidence angle and are quite different with respect to the SM derived from the L-band radiometer. These results testify that the surface roughness correction was not appropriate in either the value of the *HR* parameter and/or the power of the cosine function appearing in (2). Then, the surface roughness correction term was tuned to match as closely as possible the CORTO SM retrieval and the SM from the ARIEL data. The best value for the power of the cosine function was found to be $n = 0$ ($n = 2$ is the theoretical value).

The ad hoc roughness parameter revealed itself to be quite spread, notably more for the highest values. There is no evident correlation with the different fields or with the SM values to explain the variability of the ad hoc roughness. Of course, the anomalous values of the ad hoc roughness can be related to a wrong compensation of the vegetation effect based on the NDVI and/or to the estimation of the noise in the DDM needed to compute the reflectivity. This led to the conclusion that soil surface roughness is a key parameter to correctly estimate the SM, but in situ measurements of surface roughness are not suitable to predict the value to be used; the use of a constant value for a large region is not suitable either. The approach of forcing a tunable roughness correction per pixel is not feasible in an operational system. An alternative approach can consist in deriving empirically the best roughness parameter as a function of the incidence angle from a suitable training set. The "ad hoc" roughness derived in this way provided reasonable results and could be further exploited in the future.

The approach tested on the Balaguer data has also been applied to *TDS-1* reflectivity data collected over the REMEDHUS experimental site, where in situ SM measurements and other data are routinely collected. Similar conclusions can be outlined through the Balaguer experiment. An ad hoc roughness parameter is needed to force a correct SM retrieval. It can be adjusted locally or regionally, but this

TABLE 1. REGRESSION COEFFICIENTS AS A FUNCTION OF INCIDENCE ANGLE RANGES COMPUTED USING THE DATA SET WHEN THE RR FLAG FOR SMAP DATA IS APPLIED.

REGRESSION COEFFICIENTS FOR CYGNSS	SM	VEGETATION OPACITY	ROUGHNESS
All θ	**26.00**	–16.02	–15.22
$0° <= \theta < 30°$	**27.09**	–13.30	–16.41
$30° <= \theta < 60°$	**25.51**	–16.50	–13.50
$\theta >= 60°$	**25.66**	–21.77	–13.45

does not seem feasible (or at least it is very difficult in general and not known at present) from an operational viewpoint. For this reason, it was concluded that, at least at this stage, retrievals of spatially or temporally averaged values, possibly exploiting a temporal sequence of GNSS-R data, can be more effective.

However, recent results using airborne data acquired by a microwave interferometric radiometer over Yanco, New South Wales, Australia [76], have shown that the origin of the fluctuations of the reflectivity, mainly linked to thermal noise, speckle, and surface roughness, can be used to correct surface roughness effects. This is a new promising result that can be applied to single-pass retrievals, also from space, as in [77].

RETRIEVAL BY CHANGE DETECTION

An alternative inversion algorithm was proposed to retrieve the surface SM from CyGNSS data using a change detection approach. It was tested on the Merguellil site (Tunisia), the Dallo Basso site (Niger), and the Ouémé site (Benin) around respective ground moisture stations. As for ancillary data, 10-day NDVI products were collected and atmospherically corrected, derived from Proba-V data at a spatial resolution of 1 km. SM data (i.e., the relative saturation index, ranging between 0% and 100%), retrieved from the backscattering coefficient measured by the Advanced Scatterometer (ASCAT) radar carried aboard the *Meteorological Operational* satellite [78], were also included. CyGNSS data were filtered according to SNR >3 dB and incidence angles lower than 35°. Only data with NDVIs between 0.2 and 0.8 were considered to avoid both water bodies and dense forests; data over surfaces with altitudes greater than 600 m were also discarded. After the selection of CyGNSS data, an empirical normalization of the reflectivity as a function of the incidence angle was applied considering data aggregated on a 0.1° × 0.1° grid. Finally, data were aggregated on a 0.5° × 0.5° grid. The large dimension of this grid (e.g., with respect to the 0.25° × 0.25° ASCAT grid) is aimed at getting enough data within each pixel as specular reflections generally come from different elements of the surface and lead to a high variability in time for inhomogeneous surfaces. A minimum of five GNSS-R measurements in the same pixel was considered to derive the mean daily value.

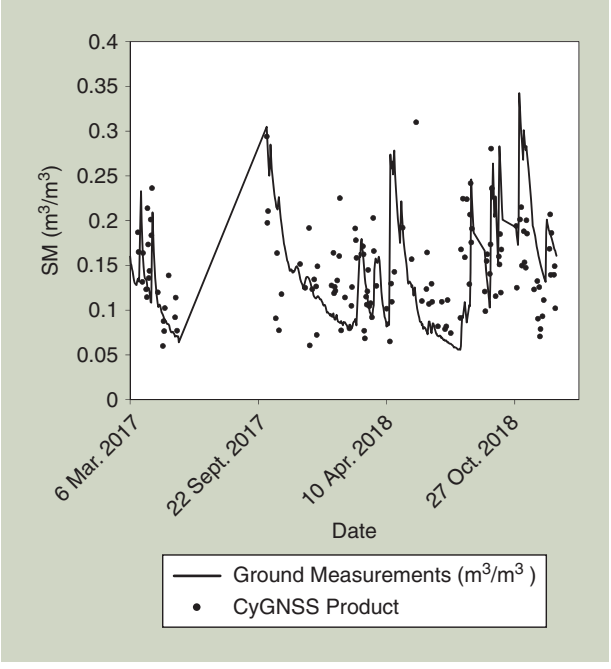

FIGURE 7. A comparison among SM products from CyGNSS data and ground measurements in the Merguellil site with the in situ probes.

A problem that was apparent looking at the data in the test area, characterized by an arid climate, is the high variation of GNSS-R reflectivity in dry conditions, with a standard deviation of about 3 dB, without any expected local effect due to the SM. This could be due to a larger uncertainty in the retrieval of reflectivity for low SNR values, but it can also be linked to the heterogeneity of the surface, both vertically (considering the high penetration depth) and horizontally, as explained before.

The change detection algorithm was applied to the data with a grid resolution equal to 0.5° × 0.5° collected during a period of 21 months. In a context of a database spanning a long time interval, the highest SM (i.e., a larger Γ) likely corresponds to soil saturation and the lowest SM (a smaller Γ) to the driest possible condition. An index between 0 and 100% is then estimated according to the following formula, referred to as the *saturation degree*, similarly to what is done for the ASCAT moisture products [78]:

$$\text{Ind} = \frac{\Gamma - \Gamma_{\min}}{\Gamma_{\max} - \Gamma_{\min}} \times 100. \tag{5}$$

Since vegetation could influence the dynamics of the reflectivity, the change detection algorithm was applied within two vegetation classes: NDVI < 0.4 and NDVI > 0.4. The number of classes could increase with the increasing length of the time series. To compare the CyGNSS saturation degree with ground measurements, CyGNSS products were converted to physical units of m^3m^{-3} by normalizing them to the mean and standard deviation of the theta probe ground data in each station.

Figure 7 provides a comparison between Merguellil ground measurements at a 5-cm depth and GNSS-R products. During the dry season, as already observed, CyGNSS retrievals exhibit a high variability in spite of the absence of temporal and spatial variation of the SM. The quality of the statistical outcome of our comparison between ground-truth measurements and satellite products is moderate. Table 2 summarizes the statistical parameters, i.e., the RMSEs and correlation coefficients. When a dry period was not considered in the proposed comparison, better results with the highest accuracy in the SM estimation were observed.

A comparison between ASCAT and CyGNSS products estimated in the period between March 2017 and the end of December 2018 was also performed. A moderate agreement between the two saturation degree products was observed (a correlation of 0.62), although one must consider the limited number of matchups and the fact that the ASCAT change detection algorithm is based on more than 20 years of radar data.

In conclusion, the use of CyGNSS data within a change detection algorithm has shown a reasonable potential for monitoring the SM content. The GNSS-R technique is still very young, and decades of experience acquired in the use of monostatic radar and passive microwaves make a great difference. Nonetheless, the accuracy was not far from that achieved by scatterometers or passive microwave radiometers. However, there are still many aspects to clarify to improve the accuracy of the estimates, such as an improved correction of topographic effects and vegetation cover, a better understanding of the limitations of low reflectivity values over dry conditions, and the need to increase the density of acquisitions as the SPs do not pertain to the same surface from one day to another. The latter factor generates a variation as a function of time over the same resolution cell of the grid, which is an issue to further consider in the future.

RETRIEVAL BY MULTIVARIATE REGRESSION

Two approaches have also been tested to estimate the SM using CyGNSS data based on an empirical multivariate regression. The results of the proposed algorithms were investigated on both a global scale and specifically over three study areas: Florida, Texas, and New South Wales [79].

Besides five months of CyGNSS acquisitions, spanning from April 2017 to August 2017 (L1 products, version 2.0), the investigation considered as ancillary data the SMAP L3 products to gather reference SM as well as information about vegetation opacity (the VOD) and the roughness coefficient.

It is worth noting that the roughness coefficient is a parameter essentially derived from information about land classification and, as such, is not very representative of the small-scale roughness. The SM extracted by the SMOS L2 product (version 6.50) was also used and was limited to the Florida, Texas, and New South Wales areas. The in situ daily SM measurements were analyzed over Florida and Texas and were taken from the Soil Climate Analysis Network (SCAN) climate monitoring stations,

The algorithm is based on a multivariate linear regression that estimates the SM as

$$\mathrm{SM} = a \cdot \Gamma'_{\mathrm{dB}} + b \cdot \mathrm{VOD}' + c \cdot \mathrm{H}' + d. \tag{6}$$

With respect to (2), the VOD, the measured reflectivity, and the roughness parameters were standardized [for this reason, they are indicated with an apex in (6)], imposing the dynamic range of the variables to be [0 1], and the dependence on the incidence angle was not considered. The standardization aims at directly comparing the weights that the retrieval algorithm gives to each variable. The regression coefficients were estimated from a combined training set of CyGNSS reflectivities and SMAP SM and then tested on an independent set. The test set was extracted randomly from 2.5 months of data, while the algorithm performances were evaluated from the remaining 2.5 months of data. The data were quality controlled to check that the CyGNSS reflectivities were positive, the VOD and roughness coefficients had valid numbers, and the acquisition altitudes were lower than 500 m. The reflectivity was then gridded for each day and over the SMAP EASE-Grid at a 36-km × 36-km resolution.

The so-called *relevance vector regression* (*RVR*) retrieval algorithm determines a unique set of regression coefficients on the global database of CyGNSS and SMAP data implementing a trilinear regression to estimate the SM. The consideration of the incidence angle in the regression model was proved not to be effective in terms of retrieval performance, and it was not included. The algorithm applied to global data tends to give similar weights to both the reflectivity and the vegetation opacity. Moreover, it tends to underestimate a high SM and overestimate a low SM. This is a typical behavior of linear regression approaches that do not account for nonlinear effects and are biased by an inhomogeneous distribution of the value of the target parameter in the training set. For this reason, a further bias correction was applied to the retrieval using a lookup table (LUT), as detailed in [79].

Figure 8 shows a density scatterplot in log scale of the SMAP reference SM and CyGNSS SM. The density plot highlights the overall good agreement between CyGNSS and SMAP, even though there is a large amount of scatter in the data. The RMSE calculated over the test set is 0.08 $\mathrm{cm}^3/\mathrm{cm}^3$ with a negligible bias. Both the bias and the RMS difference increase for increasing SM.

The RVR algorithm can also be applied on a regional scale, and the three case studies of Florida, Texas, and New South Wales were considered. The coefficients as well as the correction LUT were derived from the training data pertaining to each specific region. In this case the coefficients give more weight to the CyGNSS reflectivity in some cases and less weight in others. The test results were in line with the global case, exhibiting comparable results for Florida (RMSE 0.08 $\mathrm{cm}^3/\mathrm{cm}^3$) and much better results in Texas (RMSE

TABLE 2. STATISTICAL PARAMETERS OF THE COMPARISON BETWEEN SATELLITE PRODUCTS AND GROUND MEASUREMENTS.

SITE	RMSE ($\mathrm{m}^3/\mathrm{m}^3$)	R^2
Merguellil	0.067	0.36
Dallo Basso	0.018	0.68
Ouémé	0.051	0.7

0.06 cm^3/cm^3) and New South Wales (RMSE 0.06 cm^3/cm^3). Florida was found to be a quite problematic area for SM retrieval, even for the SMAP mission, because of the large number of lakes and swamps (bodies of water).

The retrievals from CyGNSS were also compared with L2 SMOS data for Florida, Texas, and New South Wales, also gridded daily over the EASE-Grid, at a resolution of 36 km × 36 km, to facilitate the comparison. The results (not shown here, more details can be found in [79]) were slightly worse than those for the tests using SMAP, but this was expected because the regression was trained on SMAP data. Thus, overall, the SMOS comparison showed good consistency with the previous one.

The second approach for retrieving the SM from CyGNSS consisted in estimating the regression fit between the CyGNSS reflectivity and the SMAP SM for each pixel of the considered grid. In this case, a simple linear regression using only the CyGNSS reflectivity was performed, as the vegetation opacity and roughness coefficient gathered from the SMAP products do not exhibit a temporal dynamic in a single pixel but are almost "static" parameters. This is quite understandable for roughness, but the same situation was also observed for the VOD as, in the considered SMAP product, VOD was auxiliary data, not retrieved from the radiometer observations. This does not happen on a global scale as the spatial variability of those parameters is meaningful. In the pixel-by-pixel approach, the difference in the surface conditions, other than SM, are implicitly accounted for by the different regression coefficients. Here, the pixel is chosen to be 1° × 1° of latitude/longitude since this was a good compromise between the accuracy of the retrievals and the need to have a large enough number of samples in each pixel to form the two separate subsets of training data and test data, as for the RVR algorithm. The coefficient of the linear regression for each pixel was derived from a training set, e.g., a random half of the data falling into that pixel, and the algorithm performance was estimated using the test data, e.g., the other half. In principle, this algorithm can be applied considering even smaller pixels, if more data are available. This methodology is mathematically equivalent to the approach presented in [35]. A difference between the two approaches is the use in our case of the reflectivity as an observed quantity instead of the SNR.

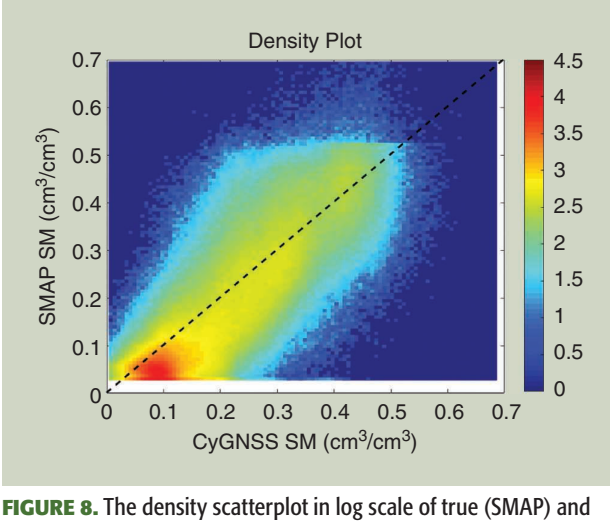

FIGURE 8. The density scatterplot in log scale of true (SMAP) and retrieved (CyGNSS) SM using the RVR algorithm on a pixel base. (Source: [78].)

The test of the retrieval on a global scale assuming the SMAP SM as ground truth is presented in Figure 8. The density plot highlights a good agreement between CyGNSS and SMAP, and the agreement is slightly improved compared to the RVR results, exhibiting on a global scale an RMSE of 0.06 cm^3/cm^3, which is close to the typical RMS differences obtained by other satellites. On a local scale, the performance in Florida was the worst (RMSE 0.09 cm^3/cm^3); it was slightly better in Texas (RMSE 0.05 cm^3/cm^3). The comparison with SMOS data confirmed the previous considerations.

Finally, the results from CyGNSS were compared with the SM measured by in situ SCAN stations over Florida and Texas and in the Merguellil catchment in central Tunisia. The estimates provided from SMAP were also considered for comparison. Both retrievals were mean daily quantities that were extracted in the pixels closest to the in situ probe location. Unfortunately, this analysis did not provide reliable conclusions. In some cases, the number of matchups was quite small, or the dynamic range of the observed SM was very small; compared to SMAP, CyGNSS exhibited retrievals that were sometimes better and sometimes worse. In general, the performances were not good, and SMAP outperformed CyGNSS for higher SM values.

SENSITIVITY TO VEGETATION BIOMASS

The sensitivity of *TDS-1* to the forest parameters related to biomass was evaluated on five test areas chosen as representative of the most important forest types on Earth: Brazil (Manaus), Uruguay (Algorta), Alaska (Fairbanks), Finland, and Argentina (Asuncion). *Advanced Land Observing Satellite* (*ALOS*) radar images have also been considered for comparison, and the sites were chosen with an extension of approximately 350 km × 350 km, corresponding to the size of *ALOS* ScanSAR images, except that the Uruguay one had an extension of 70 km × 70 km. In addition to *ALOS* backscatter images, additional data providing forest characteristics were selected; specifically, the VOD available from the SMAP L3 products, the improved pantropical biomass map providing the AGB as illustrated in [62], and the tree height derived from the ICE-GLAS lidar acquisitions at 1-km resolution on a global scale as described in [61]. It is pointed out here that AGB and tree height were "static" data, related to a specific epoch, whereas the VOD has some temporal dynamics.

The *TDS-1* and CyGNSS sensitivities to AGB as well as *ALOS* backscatter were first evaluated by comparing the reflectivity to the improved pantropical AGB map. The

comparison on a local scale was carried out on the common data set, i.e., the month of April plus the period from July to November 2017, for the Argentina, Manaus, and Uruguay test areas. Since the AGB map is limited to +/- 40° of latitude, the boreal forests were excluded in this analysis. The AGB and *ALOS* backscatter images were resampled on a fixed grid at 5 km × 5 km by averaging all of the values in the same grid cell. The result shown in Figure 9 can be considered encouraging and confirms that the main mechanism making GNSS-R data sensitive to the biomass is the attenuation of the near-specular reflected signal from the soil due to the vegetation (more discussions and results can be found in [36]).

Although there is a bias between the two reflectivity values (to be further investigated), note that both sensors show almost the same sensitivity to AGB [$0.047 \cdot \text{dB(t/ha)}^{-1}$ for CyGNSS and $0.045\ \text{dB(t/ha)}^{-1}$ for *TDS-1*]. The same happens for the correlation coefficient, which is $R \simeq 0.4$ in both cases. It is also noticeable as the scatterplot of the horizontal–vertical normalized radar cross section of *ALOS* as a function of AGB in the range 150–400 t/ha confirms the saturation observed in many articles of the L-band backscatter signal above 150 t/ha of biomass, while Γ is decreasing almost linearly down to the maximum AGB available in the data set.

Regarding tree height and VOD, in Figure 10 the reflectivity as a function of the tree height is reported, with *TDS-1* data over the test areas and CyGNSS on a global scale. The expected linear decrease of the reflectivity when the height of trees, and arguably the biomass, increases is confirmed, with $R \simeq -0.4$ and a sensitivity of about −0.66 dB/m as for the test areas. However, with higher dispersion, the result is confirmed on a global scale using CyGNSS; in this case, $R \simeq -0.36$, and the sensitivity

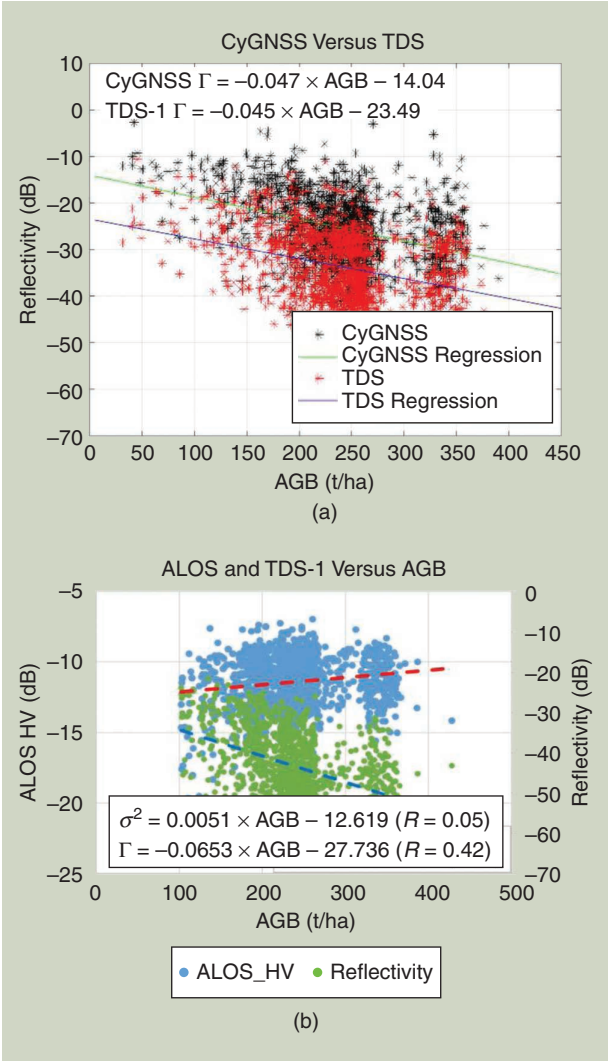

FIGURE 9. (a) *TDS-1* and CyGNSS reflectivity versus AGB from pantropical map for the Manaus, Argentina, and Uruguay test areas. (b) *ALOS* backscatter and *TDS-1* reflectivity as a function of AGB for biomass values higher than 150 t/ha. HV: horizontal–vertical.

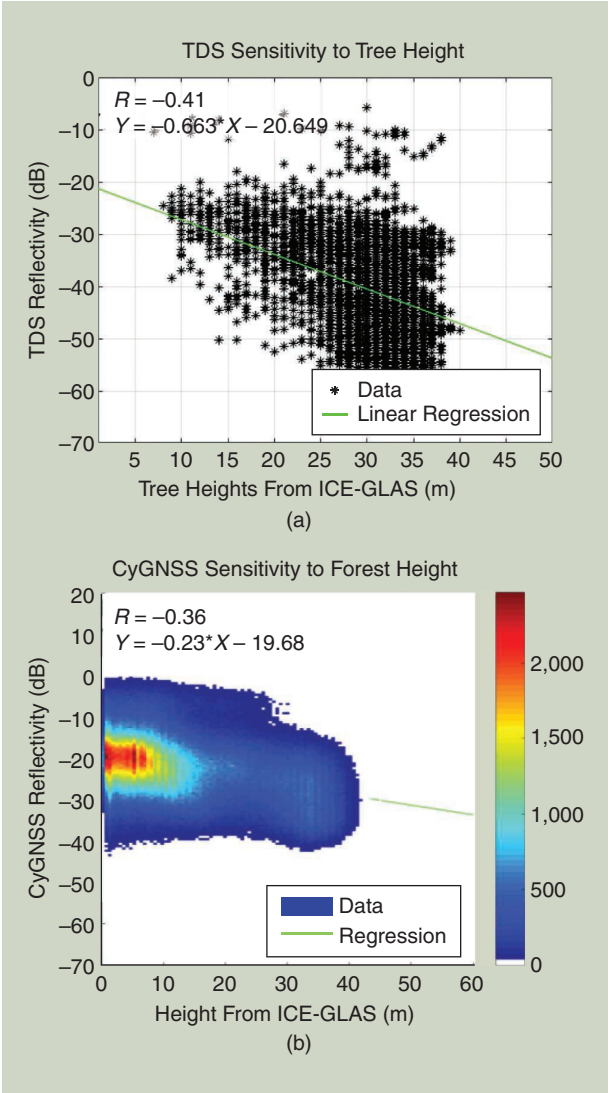

FIGURE 10. Reflectivity as a function of tree height estimated by the ICE-GLAS mission. (a) *TDS-1* over the test areas. (b) Density plot of CyGNSS on a global scale.

is –0.23 dB/m. The presence of many different species in the analysis on a global scale may partially contribute to increase the dispersion. The comparison with VOD confirmed this behavior (i.e., the negative correlation) with sometimes even better results.

Although the three parameters are not exactly providing the vegetation biomass, they are partially correlated; thus, the work provided an experimental confirmation of the biomass retrieval potential for spaceborne data. Despite the correlation staying high for large biomass values without showing apparent saturation, the SNR can become critical when the forest becomes very dense. Therefore, GNSS-R may be particularly effective for higher latitude forests, where less dense woodlands are expected, preventing a very low SNR.

To summarize, on a local scale, the observed sensitivities were 16 dB/VOD unit, 0.05 dB(t/ha)$^{-1}$, and 0.7 dBm^{-1}, for VOD, AGB, and *H*, respectively. The corresponding sensitivities at a global scale were 7 dB/VOD, 0.01 dB(t/ha)$^{-1}$, and 0.23·dBm^{-1}. Note that the sensitivities reported from two different airborne experiments were 0.015 dB(t/ha)$^{-1}$ and 0.05 dB(t/ha)$^{-1}$; thus, the present results confirm this range of values [15], [80]. The correlation coefficient is not very high, but the impact on the reflectivity of many other factors (e.g., moisture and roughness) should be considered as well as the poor temporal matching among the data (despite the expected temporal stability of the forest conditions). It is noticeable that a higher correlation was observed with the VOD at a local scale, implying a good time match between the SMAP

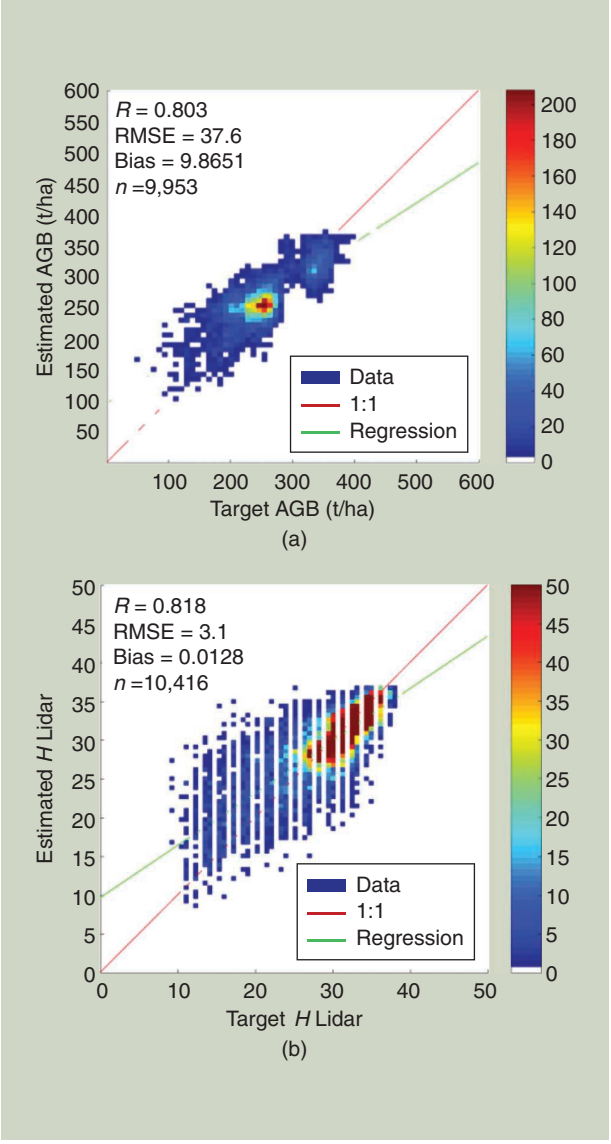

FIGURE 11. Density plots of the AGB and *H* retrieval validation on the test areas using *TDS-1* data. Density plots of (a) estimated versus target AGB and (b) estimated versus target tree height.

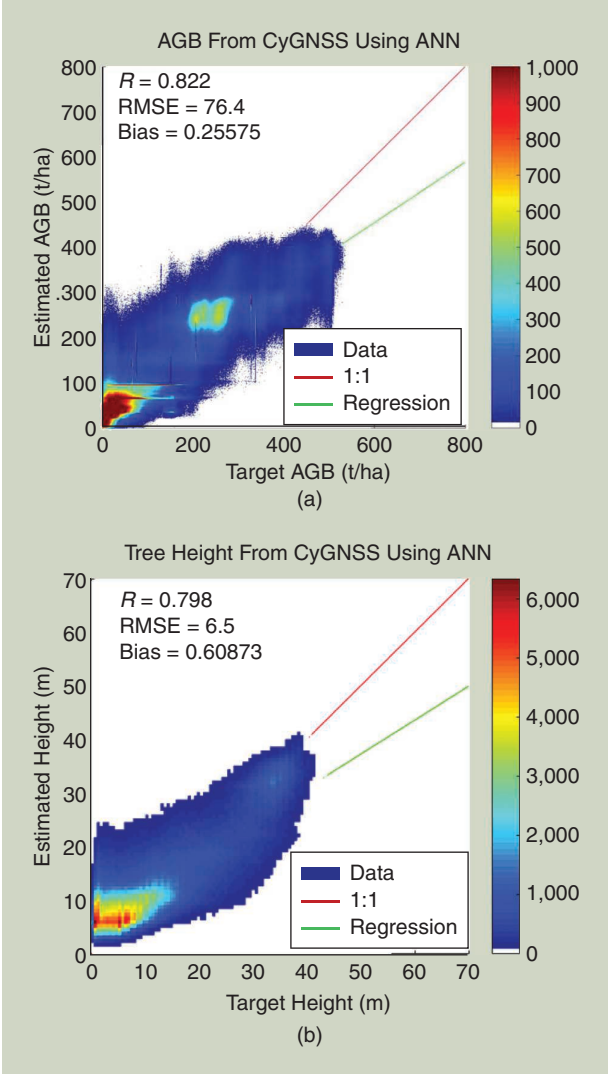

FIGURE 12. Density plots of the AGB and *H* retrieval validation on a global scale using CyGNSS data. (a) AGB estimated by ANN as a function of the reference from the pantropical map. (b) Tree height estimated by ANN as a function of the reference *H* from the ICE-GLAS data.

and *TDS-1* data, in contrast with that considering static maps of AGB and tree height.

FOREST BIOMASS RETRIEVAL

An investigation of the GNSS-R capabilities in estimating the forest biomass was carried out. To cope with the high scattering of the experimental points, prototype retrieval algorithms based on ANNs were developed [36], with the aim of estimating the AGB and forest height from Γ derived from *TDS-1* and CyGNSS alone and in synergy with *ALOS* data. Furthermore, an attempt to jointly estimate VOD and SM was carried out by using the SMAP data sets as targets for training and validating the algorithms [47]. When possible, ancillary data have been introduced in the retrieval algorithm to mitigate the ill-posedness of the inverse problem. In particular, the incidence angle has been added to the reflectivity as an input to the net; the pixel geographical location also proved a positive impact, although quite small. A synergic retrieval using both GNSS-R and *ALOS* radar data was also attempted.

Algorithms were applied to local retrievals on the selected test areas and also globally. The feedforward multilayer perceptron ANNs available in the MATLAB Neural Networks toolbox were applied. The training was based on the backpropagation (BP) learning rule. From each of the available data sets illustrated in the previous section, a subset of data was considered for training the algorithm and the remaining data for its validation. The percentage of data used for training and testing depends on the given implementation: a 50:50% separation of the data set in training and test sets was adopted for applications at local scale, because of the small amount of data available, while for the global scale it was possible to decrease the training set down to 1% of the total data set, keeping 99% of the data for the algorithm test. The network structure (i.e., the number of neurons and hidden layers and the transfer function) was defined by applying the iterative architecture definition described in [47] and [81], while the early stopping technique was used to prevent overfitting. In detail, this technique further subsamples the training set in 60%, 20%, and 20% subsets: at each training iteration the first subset is used to adjust the ANN parameters using BP, and the actual parameterization is applied to the other two and third subsets for having independent tests; training stops as soon as the errors on the three subsets begin to diverge. In general, the "optimal" ANN, depending on the given problem, was composed of two hidden layers with a number of neurons between 7 and 14, respectively, and a transfer function of type logistic sigmoid (logsig) or hyperbolic tangent (tansig).

In Figure 11 the results of two exercises conducted on a local scale using *TDS-1* data to retrieve both AGB and tree height are presented. In both cases, 50% of the data set was considered for training the ANN, and the remainder was used for validating the algorithm. Again, we note that the "static" maps (AGB or H) are not the optimal reference for comparing time series of satellite acquisitions. Nonetheless, the obtained results are encouraging, as pointed out by the value of $R \simeq 0.8$ obtained in both cases and RMSE values of 38 t/ha for AGB retrieval (in the range 100–400 t/ha) and 3.1 m for H retrieval (in the range 10–40 m).

On a global scale, the results are likewise interesting and are shown in Figure 12, where the AGB and H estimated by the ANN by using CyGNSS data are represented as a function of the corresponding target parameter. The correlation coefficients of AGB and H retrievals are good ($R \simeq 0.82$ and $R \simeq 0.80$, respectively), and the RMSE is slightly worse than on the local scale, i.e., 76 t/ha for AGB retrieval (in the range 100–500 t/ha) and 6.5 m for H (in the range 0–40 m).

The VOD and SM retrievals are shown in Figure 13(a) and (b). The statistics for VOD retrievals were $R \simeq 0.92$,

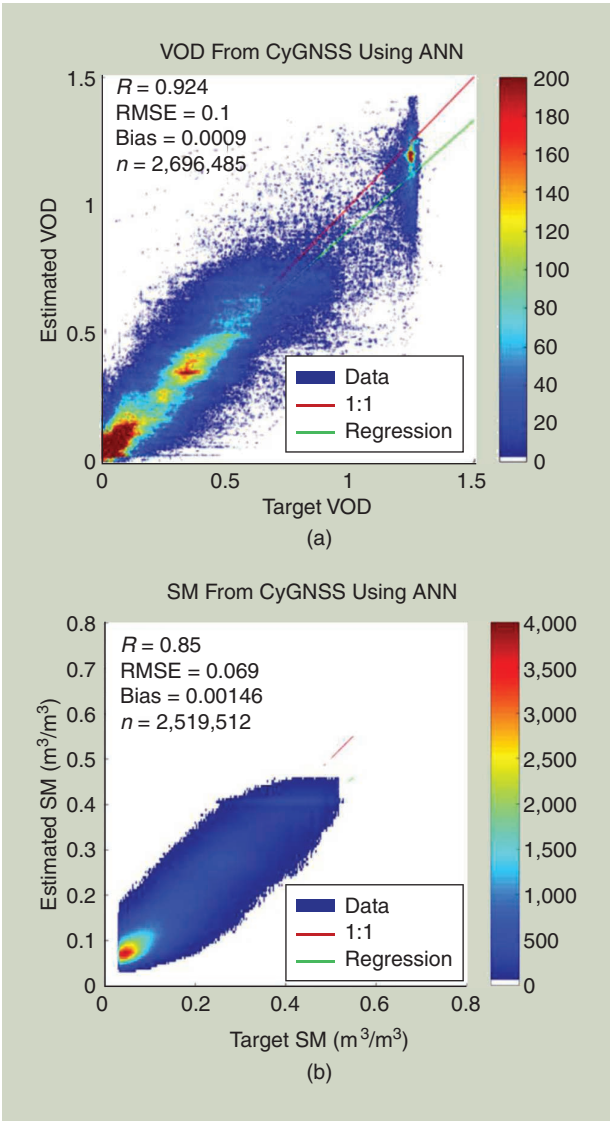

FIGURE 13. The validation of SM and VOD retrievals. (a) VOD estimated by CyGNSS as a function of the reference data from SMAP. (b) SM estimated by CyGNSS as a function of the reference data from SMAP.

RMSE = 0.1, and bias negligible; for SM retrievals, they were $R \simeq 0.85$, RMSE = 0.07 (m^3/m^3), and bias negligible. These results have been computed on a data set of about 2.6 million samples, corresponding to about six months of SMAP daily acquisitions at a global scale (from April to September 2017).

After validation, the ANN algorithms have been applied to generate global maps of forest AGB and tree height. The AGB map generated by the ANN using CyGNSS data is shown in Figure 14(a), while Figure 14(b) shows the absolute difference between the map and the corresponding target data from the improved pantropical AGB map [62], considered as a reference for implementing and validating the ANN algorithm. The agreement between the two maps is evident from the absolute error values, and the corresponding statistics are in line with the results shown in Figure 12(b). However, some local patterns with high biomass are slightly underestimated by the algorithm as can be deduced from the increase of the absolute error in some areas of equatorial forests in Africa and South America. The underestimation of the AGB values higher than 400 t/ha can also be observed in the scatterplot of Figure 12(b). This could be attributed either to the GNSS-R signal saturation for higher AGB values or to some training limit as the higher biomass values are less represented in the training set because of the limited number of samples.

In summary, the ANN estimates compared with the reference data of the test set resulted in a correlation coefficient of $0.8 \le R \le 0.9$ between the retrieved and reference quantities in the various experiments, and 37 t/ha ≤ RMSE ≤ 76 t/ha for the local and global AGB retrievals (AGB in the range 0–400 t/ha), and 3.1 m ≤ RMSE ≤ 6.5 m for the tree height retrieval (H in the range 0–45 m). Indeed, GNSS-R may have a role in monitoring forest biomass at average resolution. As we wait for the BIOMASS P-band Synthetic Aperture Radar (SAR) mission, a high-resolution product based only on satellite data with high temporal frequency is unavailable, so GNSS-R could offer the possibility of effectively covering a gap in the monitoring of forest biomass. Also, the synergy between GNSS-R and monostatic SAR is promising, as the GNSS-R sensitivity is maintained for biomass values larger than the typical saturation threshold in L-band backscatter (~150 ton/ha), provided the SNR is adequate.

INVESTIGATION ON THE FREEZE–THAW SENSITIVITY

TDS-1 data have shown that GNSS-R can have good sensitivity for freeze–thaw sensing in the active zone of permafrost [28]. Time series of monthly averaged *TDS-1* reflectivity over a grid of 36-km × 36-km cells were compared with the colocated monthly freeze/thaw fraction (FTF) product provided by SMAP, grouped in LC types.

The results showed a strong agreement between the trends of the two time series for almost all of the LC classes, with the *TDS-1* reflectivity exhibiting a dynamic range of 10 dB (see Figure 15; more details can be found in [28]). Lower reflectivity values were obtained in the winter months, when the SMAP FTF product indicated a higher fraction of frozen pixels and vice versa. Two exceptions (i.e., noisy temporal trends of reflectivity) were found for two LC classes: grassland and forest evergreen. The first case can be explained by the less marked discrimination of freeze/thaw conditions in areas located at lower latitudes. The second case can be explained by the attenuating effect of the vegetation on the GNSS-R signal.

Throughout the project, additional analyses were carried out to compare 1) the spatial patterns of GNSS-R and SMAP FTF gridded data

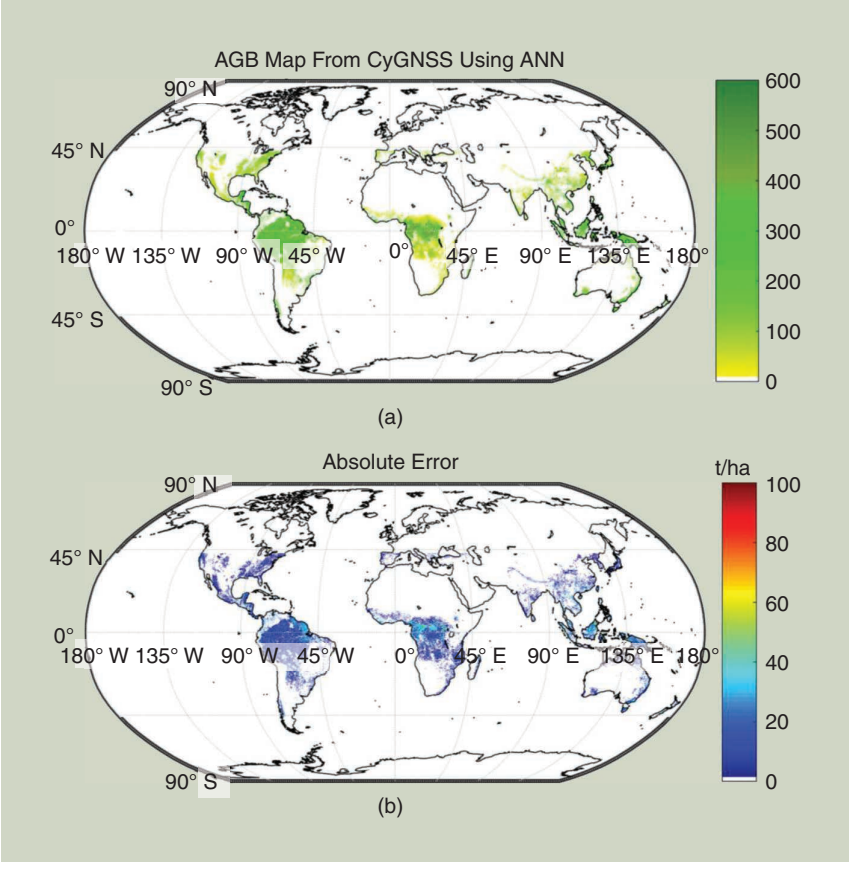

FIGURE 14. (a) Global biomass map at 5-km resolution obtained from CyGNSS data by using the ANN algorithm and (b) absolute difference between the map and the improved pantropical AGB [61], considered as reference.

(36 × 36 km) and 2) GNSS-R and in situ temperature data. In both cases, the GNSS-R sensitivity to frozen soil conditions was highlighted. In particular, the comparison with in situ data collected by stations located in Canada, Finland, Siberia, and Alaska showed that the anomalies (i.e., deviations from the temporal average value) in *TDS-1* reflectivity data were correlated with the in situ soil temperature. Negative anomalies can be associated to frozen soil conditions, whereas positive anomalies align with thawed soil conditions. Transitional seasons (in which the average temperature ranges between –2 and 2 °C) and months characterized by higher NDVI values produced results with a higher degree of uncertainty (a lower correlation between GNSS-R reflectivity and temperature). More details about this analysis can be found in [28].

SIMULATOR UPGRADE AND VALIDATION

GEROS

In this project, the GARCA/GEROS-SIM4LAND software packages have been implemented, starting from the GARCA/GEROS-SIM OCEAN version, which simulates the spaceborne GNSS-R observables (DDM and waveforms) over ocean [48]. Many parts were directly reused without modifications, for example, the DDM generation module. However, some parts were modified according to the mechanisms of GNSS-R signal reflection and scattering over land. The simulator operates according to two simulation modes: 1) the parameter sweep mode and 2) the orbital propagation mode with an inhomogeneous field of view (FOV). More details can be found in [49].

The static mode simulates the DDM, varying a single input parameter and holding the other parameters constant. This mode is efficient for studying the impact of a single parameter on the DDM. In the static mode, the specular reflection point is set as user input (lat, lon). Other user inputs for this mode are the receiver orbital height, the incident angle, and the azimuths of the transmitter and receiver.

The orbit progressing mode for inhomogeneous FOV simulates the DDM according to the actual orbit progress on each epoch. To simulate an actual spaceborne GNSS-R instrument like the *TDS-1*, the transmitter and receiver states (positions and velocities) are inputs of the simulation. The geophysical data describing the earth's surface are also read from a database that was produced during the Synthetic Aperture Interferometric Radiometer Performance Simulator (SAIRPS) Radiative Transfer Module (RTM) development [34]. This mode is useful for comparing to *TDS-1* data as well as any future spaceborne GNSS-R mission. Note that the DDM output is furnished in units of received power of the down-looking antenna, assuming a nominal EIRP of the GNSS transmitters. A few examples of the simulator outputs and validation with respect to real GNSS-R data are presented in the following discussion.

An example of the simulation results of the static mode is shown in Figure 16. According to the input parameters concerning the observation geometry, SP location, and geophysical values characterizing the surface target, the simulator computes the internal variables and provides the output DDM. Figure 17 shows the result of one snapshot for the orbit progress mode. According to the transmitter

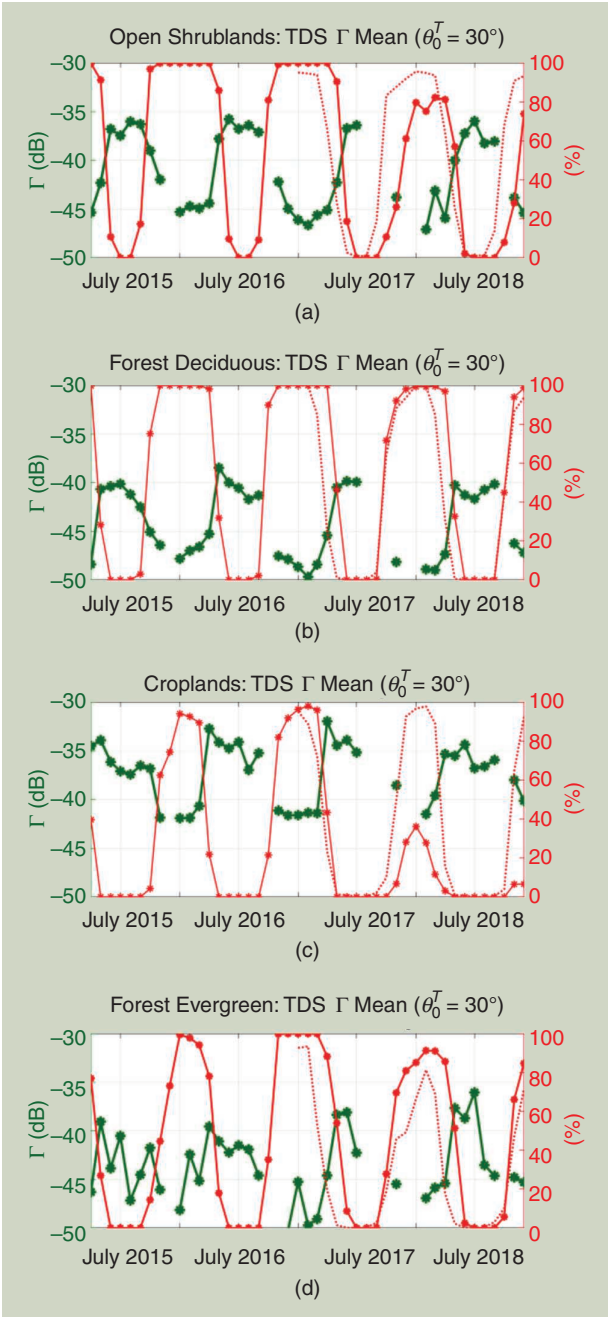

FIGURE 15. The time-series analysis of the SMAP FTF (solid red curve, right axis) and percentage of frozen pixels (dotted red curve, right axis) versus the *TDS-1* calibrated reflectivity (left axis) for relevant macroarea LC classes. (a) Open shrublands: TDS Γ mean ($\theta_0^T = 30°$). (b) Forest deciduous: TDS Γ mean ($\theta_0^T = 30°$). (c) Croplands: TDS Γ mean ($\theta_0^T = 30°$). (d) Forest evergreen: TDS Γ mean ($\theta_0^T = 30°$). θ_0^T indicates the upper bound of the considered incidence angles. (Source: [28].)

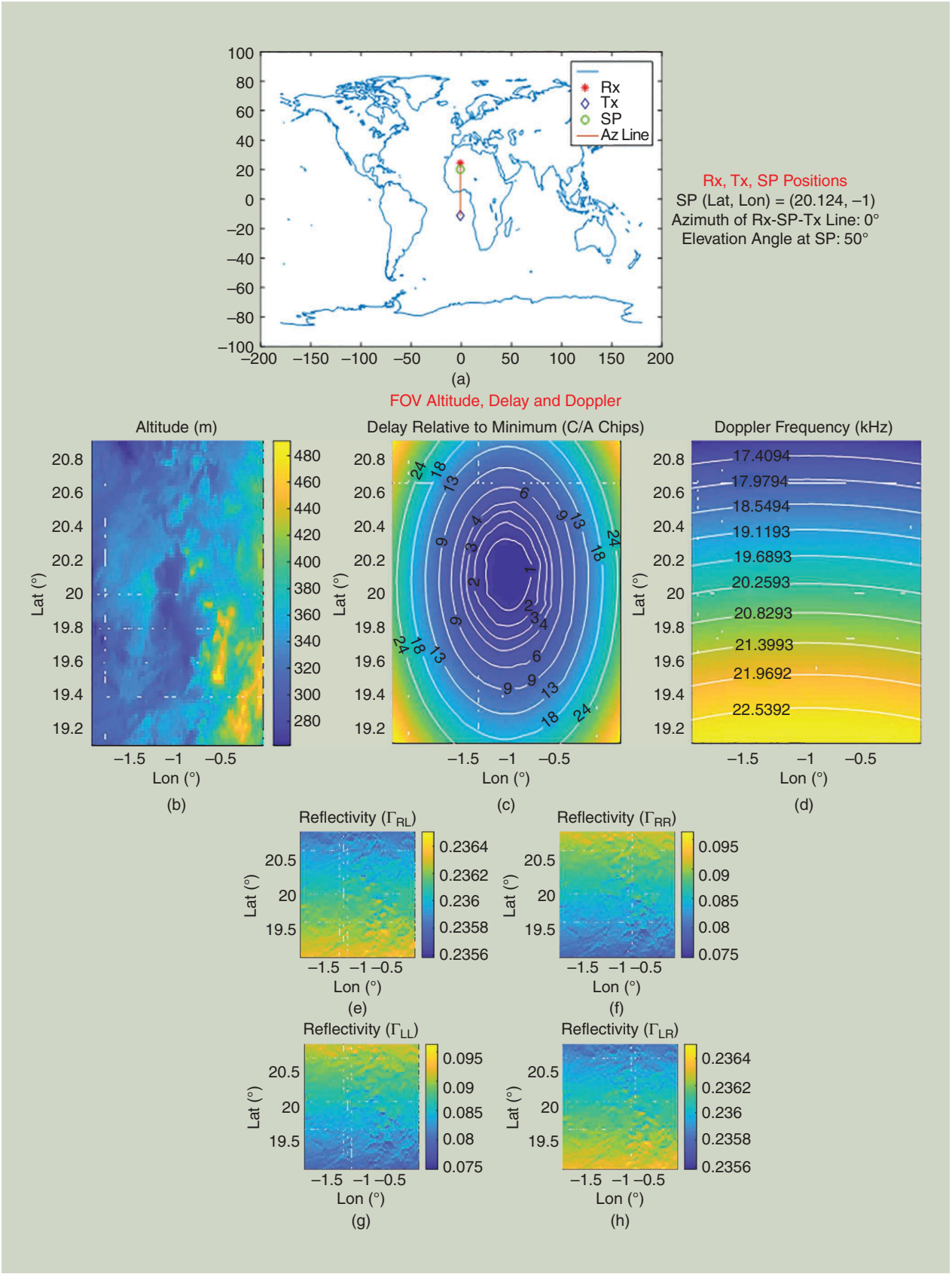

FIGURE 16. The results of the static mode GARCA simulations. (a) The positions of receiver (Rx), transmitter (Tx), and specular point (SP). (b) The altitude of glistening zone. (c) The delay with respect to the SP in coarse/acquisition (C/A) chips. (d) The doppler frequency and reflectivity in each polarization: (e) RL, (f) RR, (g) LL, and (h) LR; LR: left–right *(Continued)*

and receiver positions and velocities read from the *TDS-1* files, the observation geometry is computed, and the reflection/scattering scene is modeled using the geophysical database from the SAIRPS RTM. Finally, the DDM is computed and delivered as an output.

The static mode of the simulator is more suitable for studying the geophysical parameter impacts on the DDM with a simple sweep of the geophysical quantity. As an example, Figure 18 shows the values of DDM peak as a function of the SM. The peak value increases with the increase of SM. The slope of the curve complies with two regimes: 1) 43 dB in the SM range [0–0.15] and 2) 8.6 dB in the range [0.15–0.45]. The slope in the range [0–0.45] is 17 dB. These values are in agreement with the experimental results published in [34], i.e., 38 dB/100% for bare dry soils, and in [19], ~9 dB/100% at global scale, and they demonstrate that a higher sensitivity to SM is achieved for dry soils.

The results for the inhomogeneous FOV of the orbit progress mode were produced for different parts of the world and compared with *TDS-1* data. We only show one case over Tunisia, in a dry and flat region with a high desert fraction. Figure 19 shows the DDM peak values, which are quite weak due to the rough and dry soil. The highest value of the DDM on this area is comparable to the lowest DDM peak on more

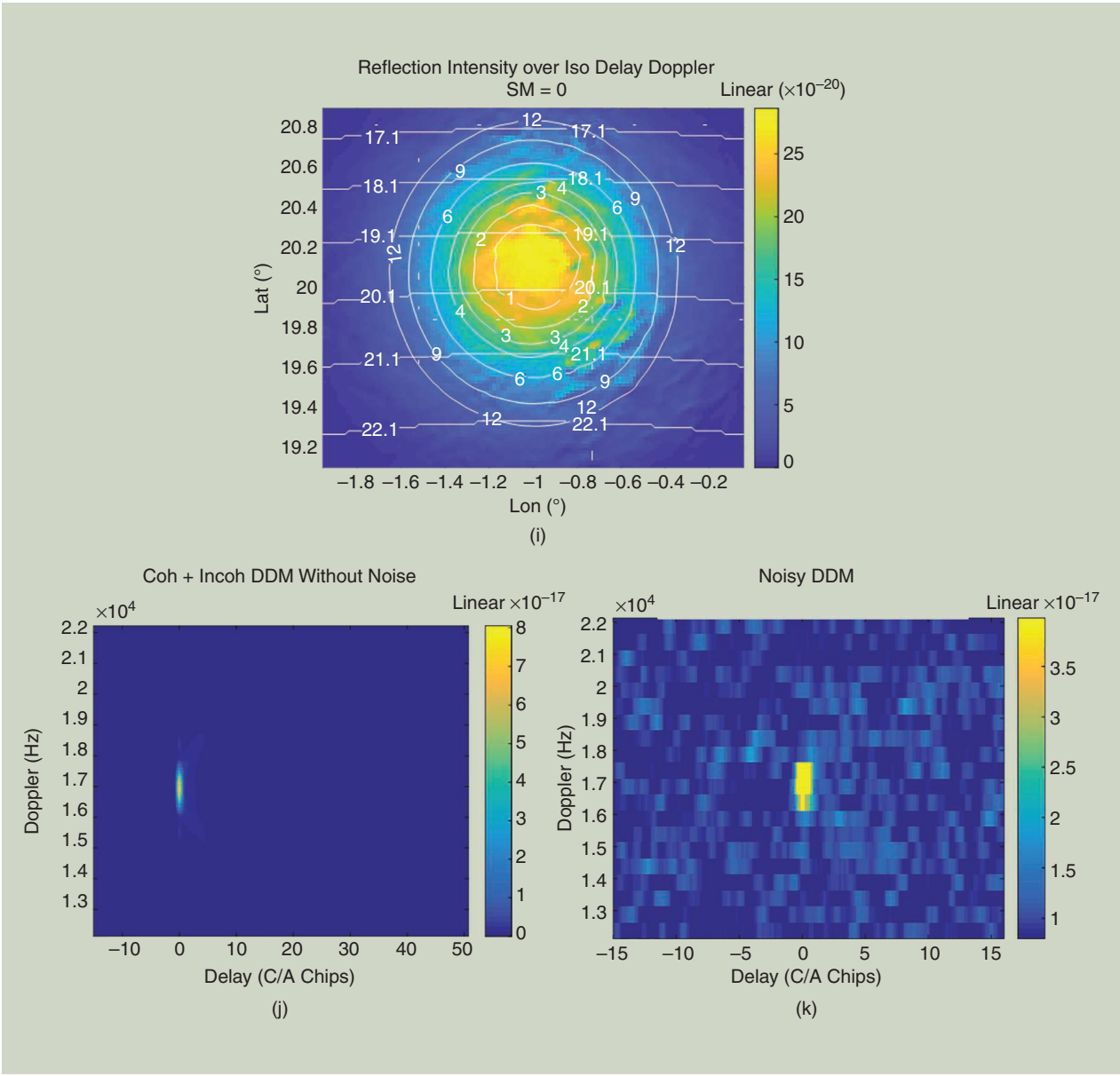

FIGURE 16. *(Continued)* The (i) equivalent reflection intensity is convolved with (j) Woodward ambiguity function producing clean DDM. Note the *K*-shape of the noise-free DDM resulting from the sum of the coherent and incoherent components (Coh+Incoh). This shape is not that clear in the (k) noisy DDM, and the incoherent term is mostly buried under the noise. Lat: latitude; Lon: longitude. (Source: [49]).

wet areas with complex topography, i.e., −169 dB_W. Both the simulation and real DDM peaks have very similar shapes but are somehow different in the middle part. There is also a peak value on the final part of the DDM peak plot, which corresponds to flat ground. A comparison between the simulated and measured power is reported in Figure 19.

In summary, the simulator has been verified and validated using the *TDS-1* data for four different cases. The simulated DDM follows the *TDS-1* DDM quite well in terms of shape in the delay-Doppler plane and peak values. The specific conditions of the FOV are also reflected in the simulated DDM, e.g., dry and wet, desert and forest, inland water, and coast. The GARCA/GEROS-SIM4LAND simulator is available online at http://147.83.91.189/.

SAVERS

SAVERS was conceived as a simulator of a GNSS-R instrument response able to incorporate the most accurate

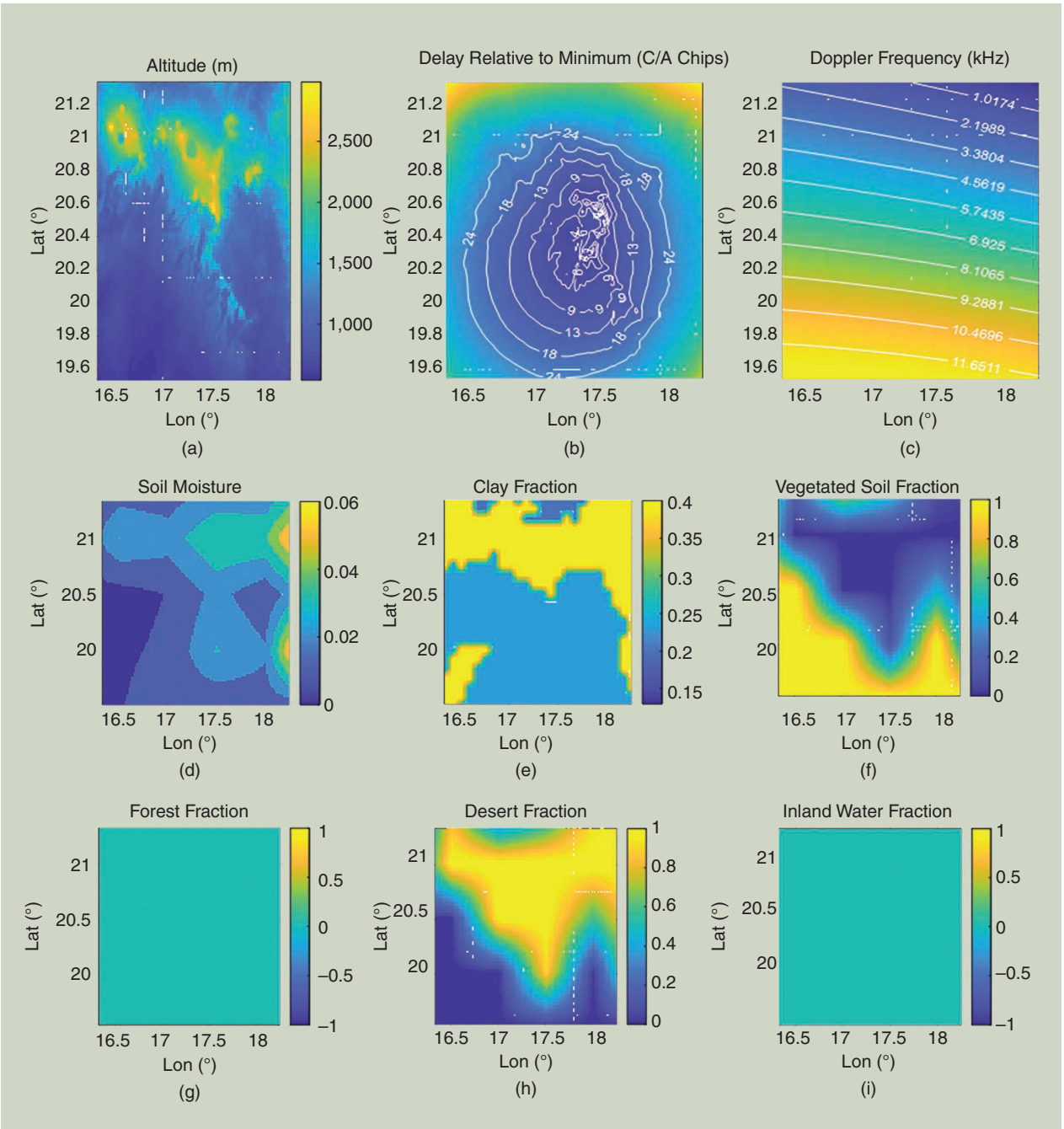

FIGURE 17. The input data and results of the orbit progress/inhomogeneous mode GARCA simulation: (a) altitude, (b) delay, and (c) Doppler frequency over glistening zone. Geophysical parameters: (d) soil moisture, (e) fractions of clay, (f) vegetated soil, (g) forest, (h) desert, and (i) inland water. *(Continued)*

electromagnetic models of bare and vegetated land surfaces [50]. The first version of SAVERS was developed during the Land Monitoring With Navigation Signal project funded by the ESA and validated using a ground-based experimental campaign at Montespertoli, Italy [13]. It took as input the system and observation parameters as well as geophysical parameters of the soil and growing sunflower plants. During a second ESA project (GRASS), SAVERS was refined to include forest attenuation and scattering properties as well as mixed-pixel effects. It has been applied and validated in the conditions of the airborne campaign at Forcoli, Italy [15].

In this project, SAVERS has been modified to fit a satellite-borne GNSS-R configuration, specifically the observational setup of *TDS-1*, leading to the SAVERS-TDS release [51]. In particular, the main improvements consist in the introduction of the effect of topography, of a very large footprint, and the actual *TDS-1* antenna pattern. Some additional upgrades regarding the electromagnetic modeling of the coherent near-specular component were also included, as detailed in [52].

SAVERS operates similarly to the orbit progress mode illustrated with reference to the GARCA/GEROS-SIM-4LAND simulator. It provides many plots describing the geometrical and electromagnetic parameters of the scene under study, as detailed in [50]. The final outputs are the full DDMs, calibrated in terms of surface equivalent reflectivity. Their peak values can be compared directly to the *TDS-1* or CyGNSS observations.

In this article we do not provide details about the mathematical formulations implemented in SAVERS-TDS; they can be found in [50] and [51]. Rather, we provide samples of the simulator outputs, the investigation about the sensitivity of GNSS-R reflectivity to the relevant geophysical

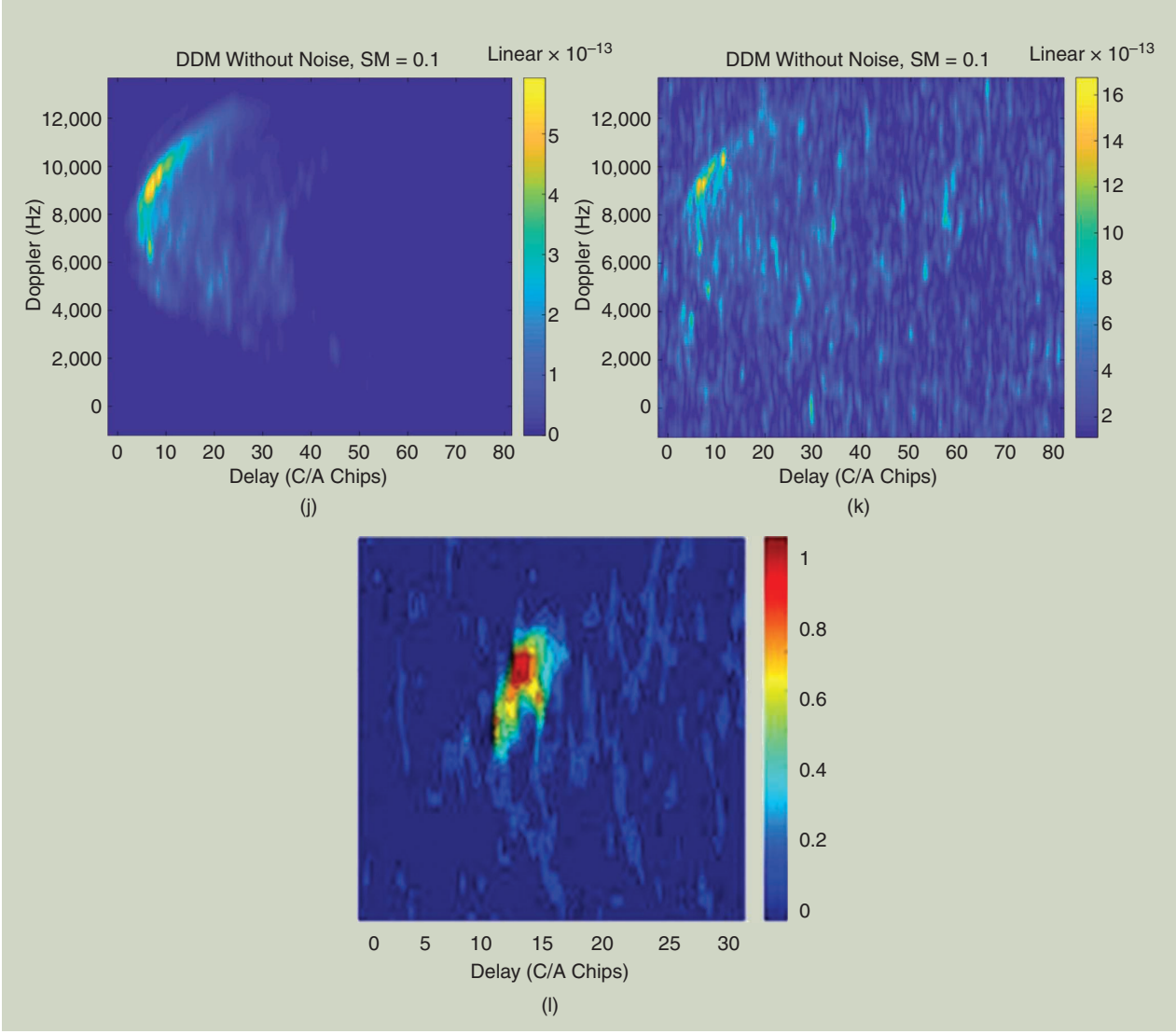

FIGURE 17. *(Continued)* The simulated DDM (j) without noise impact and (k) with noise. (l) The actual TDS-1 DDM of the same scenario (Source: [49]).

parameters enabled by SAVERS-TDS, and the validation effort based on the comparison with *TDS-1* data. The sensitivity analysis consisted in varying one parameter at a time in a selected range, keeping all the others fixed.

In Figure 20, we report the left–right (LR) reflectivity versus the SM as predicted by SAVERS. Here we show that the SM sensitivity changes according to the surface topography. Considering a real digital elevation model (DEM) of a volcanic area in Chad, we have selected two SPs at different elevations along a *TDS-1* track and plotted the reflectivity as a function of the SM. The corresponding reflectivity over a flat terrain [the top blue line in Figure 20(a)] is reported as a reference; the small-scale roughness was set to 1.5 cm with no vegetation on top. It is possible to observe that the sensitivity to SM is quite independent of the surface elevation, though the LR reflectivity gets lower as the elevation gets higher.

In Figure 21, the sensitivity to forest biomass is compared for SPs at different heights along a *TDS-1* track over the same mountainous terrain. For ease of reference, the same geographical locations as in Figure 20 have been selected, though it is not actually a forested site. The biomass variation was set in the range [25÷400] t/ha, which is linked to a variation of the mean diameter at breast height within the range [7÷21] cm and of the density within [350÷100] trees/ha through the allometric equations in [64]. The reflectivity corresponding to a flat terrain is reported as a reference [the top blue curve in Figure 21(a)]. It can be observed that the sensitivity to biomass decreases over areas with an important topography. Since the elevation decreases the reflectivity value, the coherent scattering may eventually become weaker than incoherent scattering from the vegetation volume and underlying soil. In this case, the saturation threshold is reached, as happens in the monostatic case, and the sensitivity to biomass may be lost. We remark that SAVERS is able to model not only the attenuation contributions connected to the VOD, but also the volume scattering from the vegetation canopy [38].

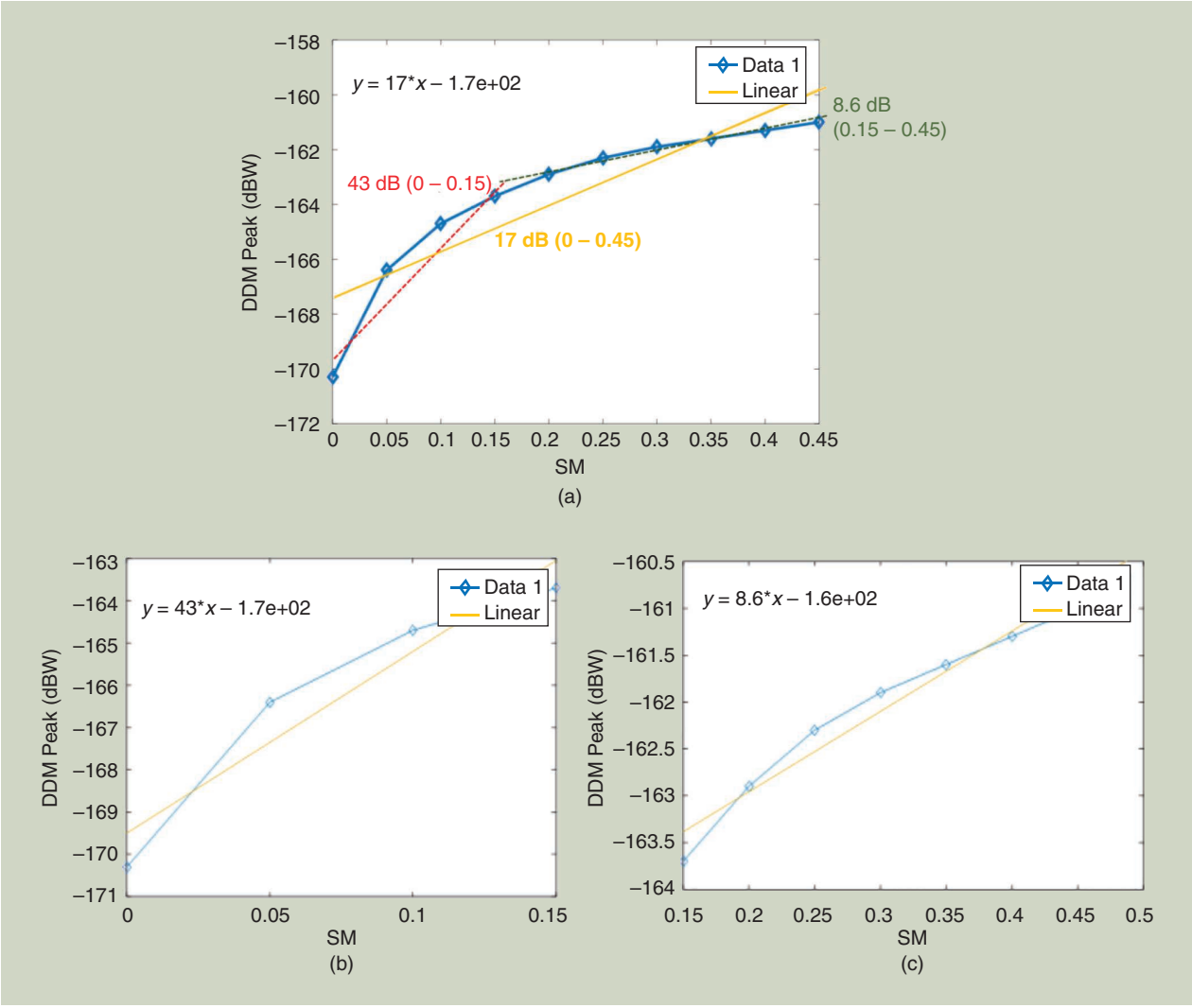

FIGURE 18. The simulated DDM peak values with GARCA as a function of SM. (a) Simulation over the entire SM dynamic range (from [49]) and corresponding mean sensitivity are compared to the sensitivity estimates for (b) small and (c) large values of SM.

The reliability of SAVERS was evaluated over bare areas with a complex topography and over forested areas, by comparing the simulator output with *TDS-1* data. The resolution of the DEM was demonstrated as having an impact on the simulation accuracy. As a tradeoff between accuracy and computational time, a 300 m spaced DEM is the best choice [51].

In Figure 22(a) and (c), the measured DDMs are shown, and Figure 22(b) and (d) depict the ones simulated by SAVERS (using a 100-m resolution DEM) for two acquisitions along a track overpassing the Chad volcanic area as in the previous examples. The data collected over a complex topography are characterized by a noisy DDM, where a clear pattern is less recognizable, and several peaks are spread in the DDM. Note that the shift of the DDM peak in the Doppler domain was found both from the data and the simulations, and it was opposite for the cases of the receiver leaving the mountains [positive Doppler shift, as in Figure 22(a) and (b)] or approaching them [negative Doppler shift, as in Figure 22(c) and (d)].

A quantitative comparison of the peak reflectivity measured by *TDS-1* and simulated by SAVERS along the same orbit is shown in Figure 23, where the profile of the surface height is also reported. It is interesting to note the large difference in reflectivity associated to the topography. Much smaller values occur over the higher terrain, where many DEM facets with different orientations can contribute to the signal, and none of them produces a strong specular reflection as in the case of an infinite-plane surface. Note that the small-scale roughness was not known in the area, and so its value was selected in the order of 3.5 cm. The value of the roughness height standard deviation shifts the reflectivity profile up or down, but the dynamic range of the reflectivity due to the topography along the track is notably reproduced by SAVERS.

A similar comparison was carried out over forested areas. Figure 24 compares the measured and simulated peak reflectivities along a track overpassing a forested area near the border between Congo and Zambia. The tree height, as provided by lidar data [61], is included in the

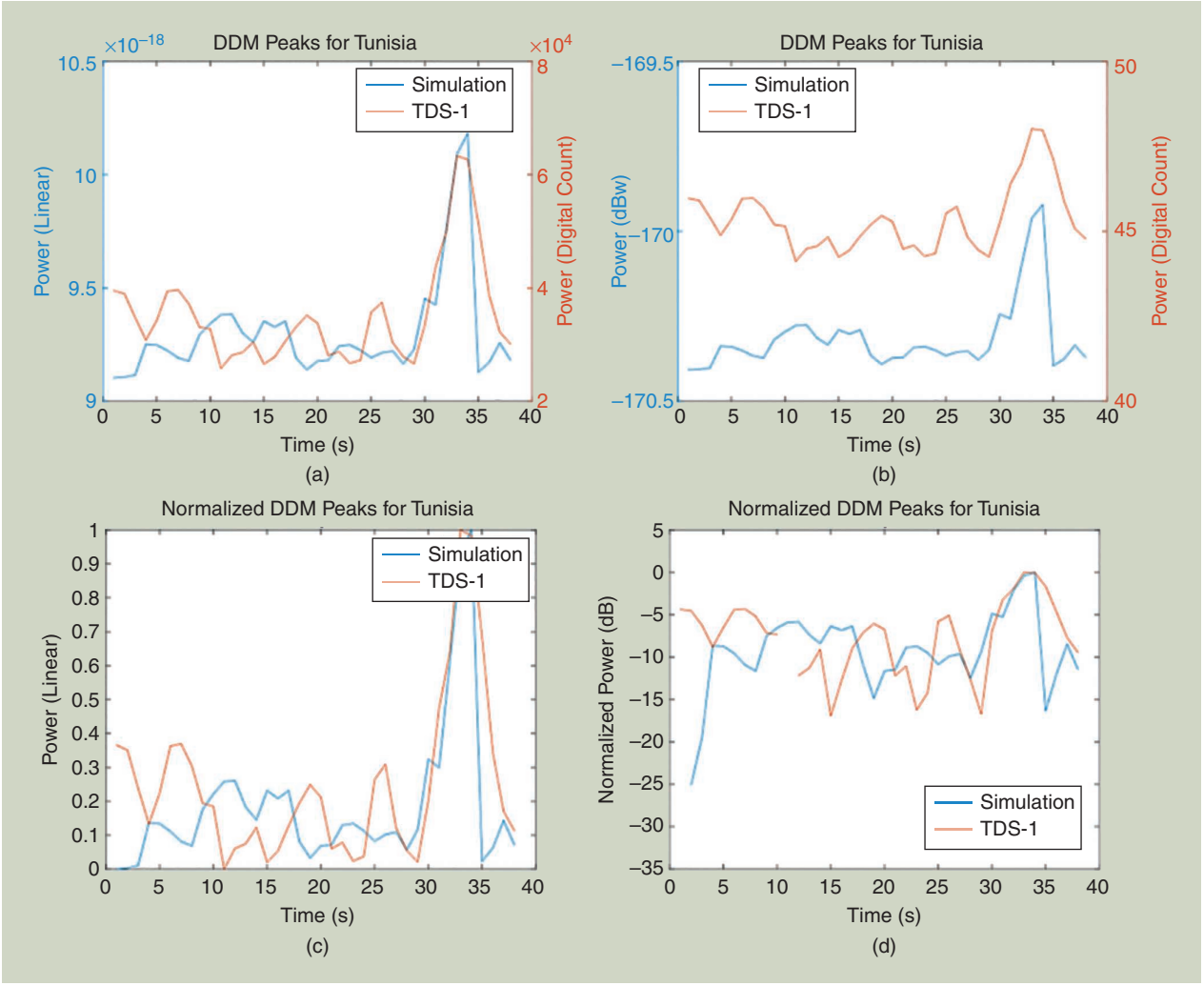

FIGURE 19. The DDM peak values for Case 1, Tunisia: (a) and (b) GARCA simulated power and *TDS-1* digital count; (c) and (d) normalized values. (Source: [49].)

plot as an indicator of vegetation biomass along the track. The simulated reflectivity corresponds to a mean biomass of 100 t/ha, and its trend is smoother than the observed one as it underestimates the higher reflectivity and overestimates the lower reflectivity values, with an R^2 of 0.23 and an RMSE of 3.15 dB. However, the lidar tree height shows an inhomogeneity of the vegetation along the track. In particular, the area between −10.2° latitude and −9.6° latitude is characterized by taller trees and, consequently, a higher biomass than the rest of the track. By contrast, the peak at −11.4° latitude corresponds to a minimum of tree height, so that it is very likely due not only to a topography effect but also to a very low biomass or bare surface. Therefore, it is realistic to assume that the biomass is variable

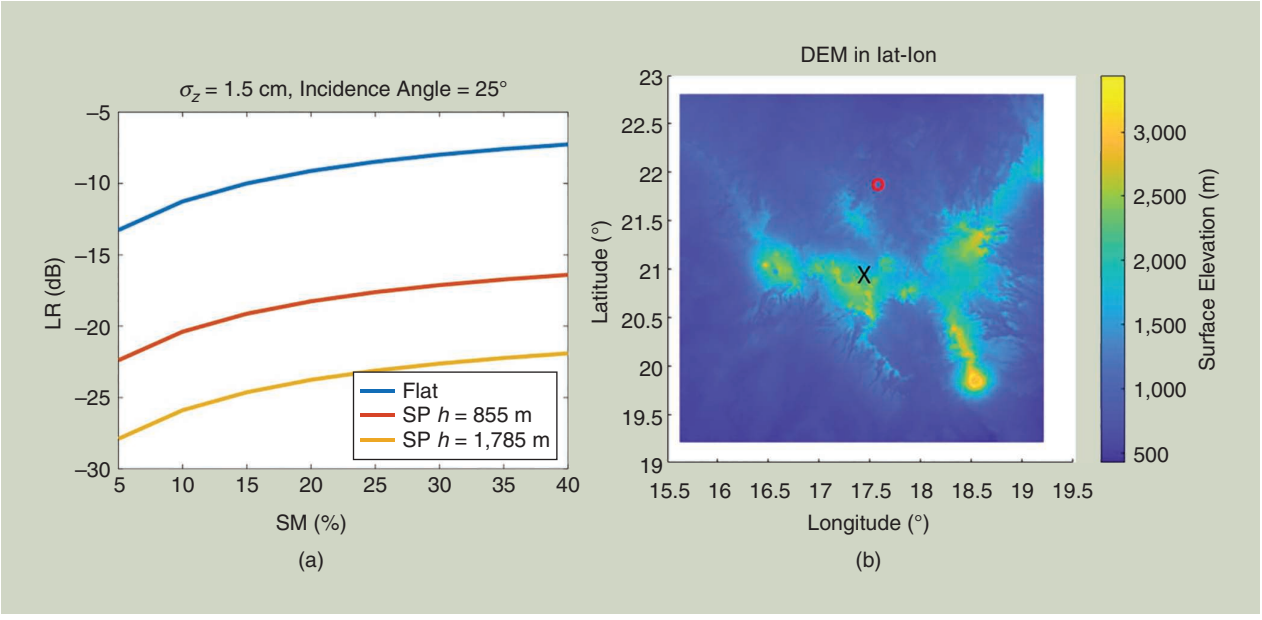

FIGURE 20. The SAVERS simulated reflectivity at LR polarization versus SM for a height roughness standard deviation of $\sigma_z = 1.5$ cm and an incidence angle of 25°. (a) Different colors represent different topographic elevations of the SP. (b) The real topographical relief was provided by the Shuttle Radar Topography Mission (SRTM) DEM. The circle and cross correspond to the positions of the SP of the simulations at different elevations. LR: (left–right);

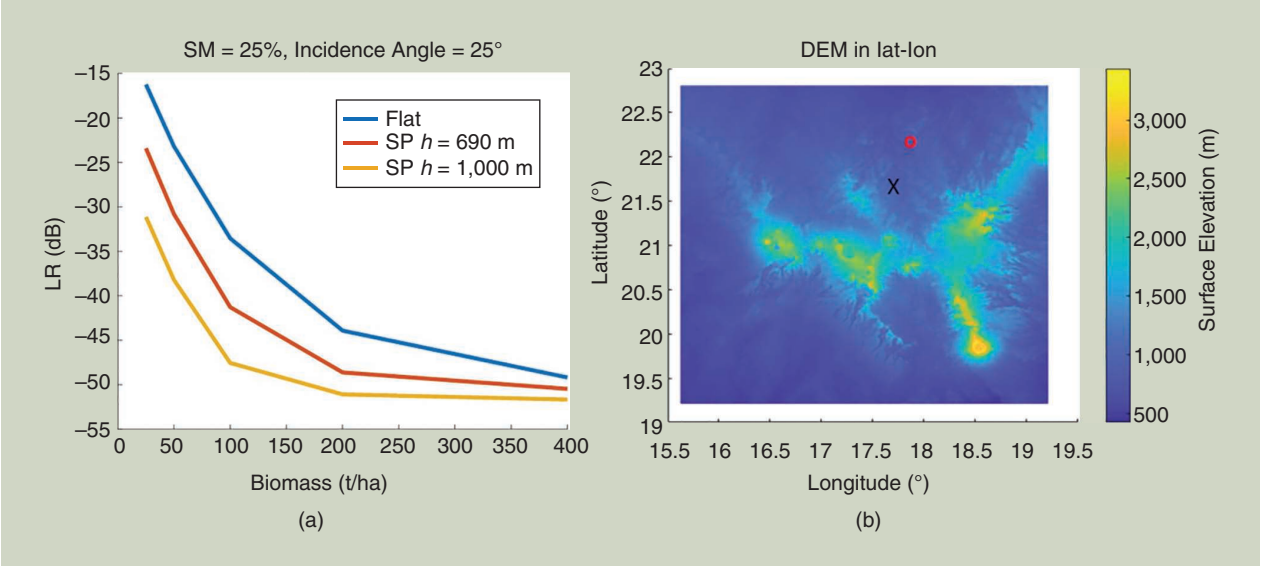

FIGURE 21. The SAVERS simulated reflectivity at LR polarization versus forest biomass, for a height roughness standard deviation of $\sigma_z = 1.5$ cm and SM = 25 %. (a) SAVERS simulated reflectivity versus biomass for a real topographical relief and an incidence angle of 25° (different colors represent different heights of the SP). The SRTM DEM is reported in (b). The circle and cross correspond to the positions of the SP corresponding to different elevations.

along the track. The error bars overlapping the simulated peak reflectivity in Figure 24 indicate the reflectivity variations if the biomass ranges from 80 t/ha to 120 t/ha.

The low values of reflectivity measured by *TDS-1* would not have been reproduced without the consideration of the forest attenuation that was predicted by SAVERS using suitable allometric relations associating a value of the biomass to the height measured by the lidar. A careful analysis of this data set shows that some features of the reflectivity profile were reproduced by introducing a DEM in the simulation, whereas other features were associated to a change in the vegetation, leading to an overall good agreement between simulation and measurements, at least for most of the track.

DISCUSSION AND CONCLUSION

The work carried out in the frame of an ESA-funded project, focusing on the study of the potential application of GNSS reflectometry over land, was described and summarized. The research confirmed previous findings about the sensitivity of the reflection to land biogeophysical parameters, i.e., SM and forest biomass. It confirmed, coherently with other works from the literature, that the sensitivity to the target parameters can be considered well established and quite promising, even in the case of satellite observations. It is noticeable that the "average" behavior of the signal (i.e., its trend as a function of the target parameters once any other effect is properly smoothed out) is also quite well reproduced by models. The increase of reflectivity with SM, which is due to the increase of permittivity, and its decrease as a function of the forest biomass due to attenuation of the coherent soil reflection, are reproduced by models if the coherent and incoherent contributions to the signal and the effect of topography are properly considered.

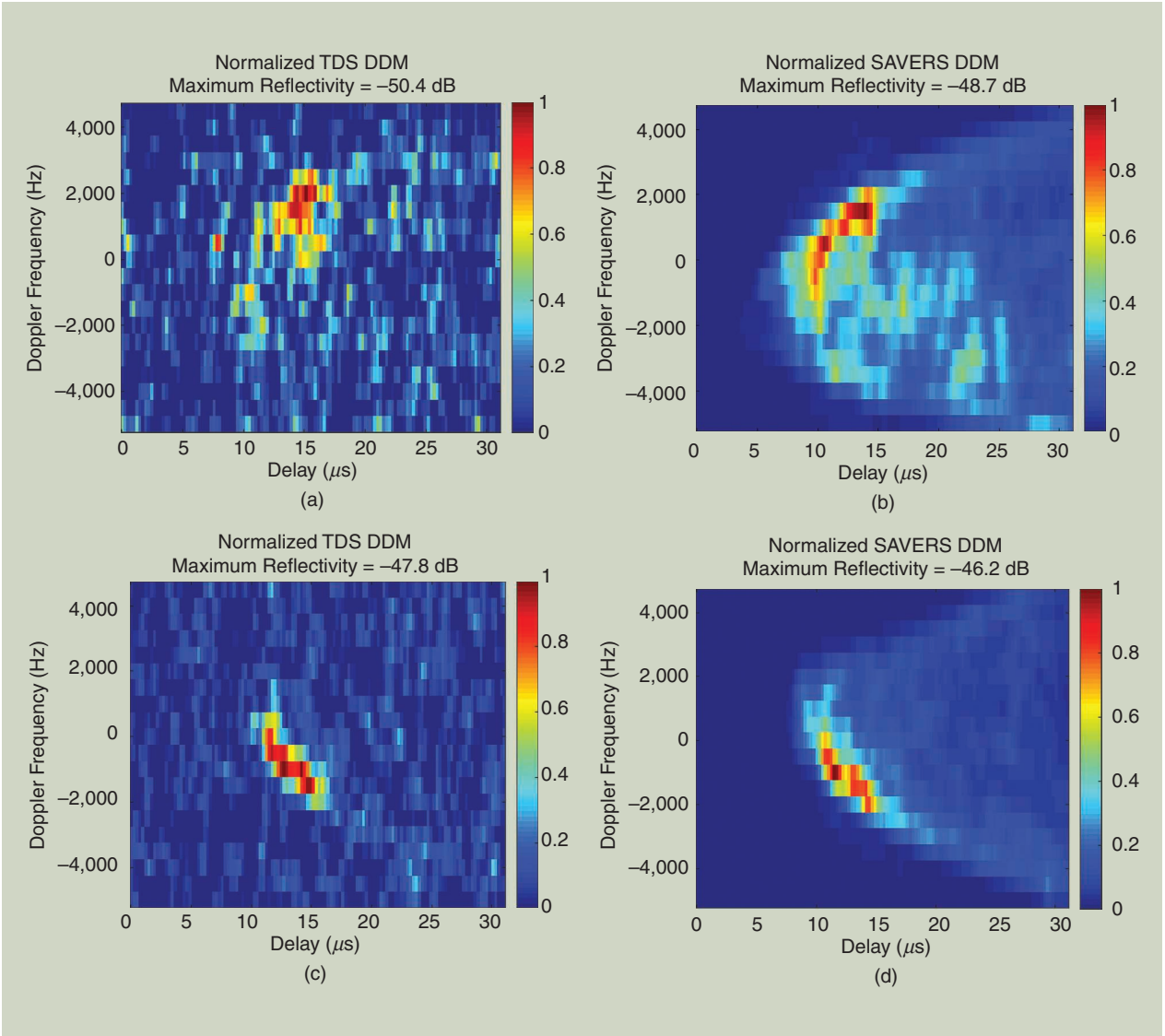

FIGURE 22. (a) and (c): *TDS-1* DDM normalized to maximum. (b) and (d): SAVERS DDM with 100-m DEM resolution. (a) and (b): SP at 20.22° latitude. (c) and (d): SP at 21.89° latitude. (Source: [51]).

Tables 3 and 4 summarize the sensitivities derived from the different experiments and model predictions carried out during the project. The results are quite consistent, with the airborne data exhibiting a higher sensitivity but referring to drier conditions.

The impact of topography is clearly highlighted by the work, both experimentally and from the models. There was a consensus in the need to upgrade the simulation models introducing the topography effect when predicting the signal from satellites.

The spatial resolution can also be good (on the order of kilometers) for very flat surfaces if the signal is mainly coherent; otherwise, it goes down to about 25 km. However, the measurements are sparse (they are not arranged as in one image), and they are not characterized by exact and fixed repetition cycles. Thus, some aggregation in space and time must be carried out to obtain a product having a raster (i.e., a gridded) format. The GNSS-R technique is also affected by a poor coverage and temporal resolution. As a matter of fact, an SP for repeating passes is located in different positions so that, for inhomogeneous targets, this can generate a variable signal as a function of time. For these reasons, a constellation of small satellites must be considered to overcome the problem [39], [72].

The work has also addressed the need of ancillary data for retrieving the target parameters to compensate for the effects of other features affecting the signal, including the small-scale surface roughness and the topography (this is, however, a common situation in remote sensing). Dual polarized GNSS-R observations have proved quite useful from low platforms but are not yet tested from satellites, except for the experiment exploiting the SMAP radar as a GNSS receiver.

In addition to the influence of many parameters on the signal and the fact that observations are not regularly repeated on the same point in inhomogeneous areas, large fluctuations (a sort of speckle) were observed, even when

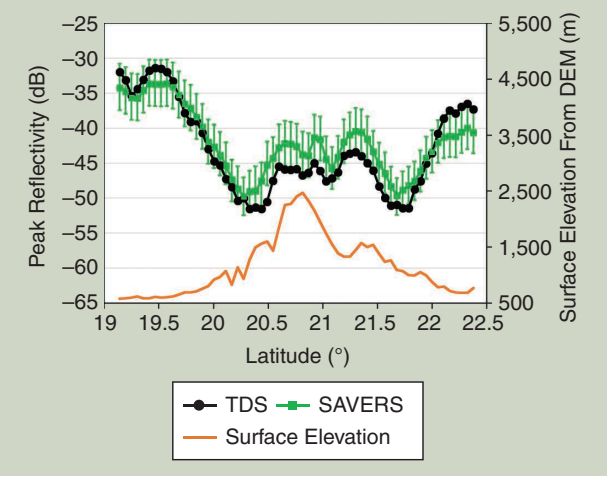

FIGURE 23. The *TDS-1* peak reflectivity compared to the reflectivity simulated with SAVERS for a bare soil. The error bars indicate the reflectivity variations for surface small-scale roughness ranging from 3.2 to 3.8 cm. The surface elevation is extracted from the SRTM DEM.

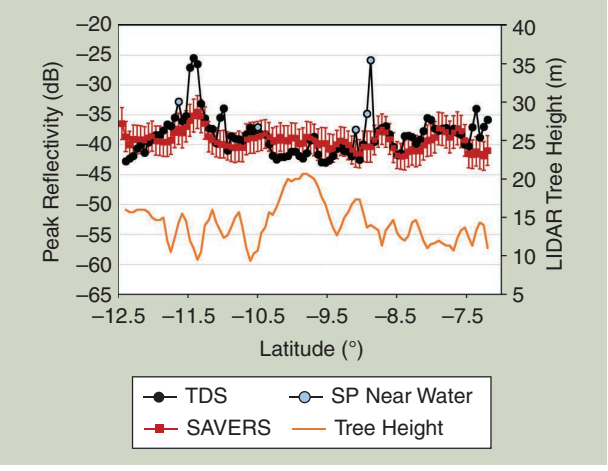

FIGURE 24. The SAVERS simulated and observed peak reflectivities versus latitude. The error bars indicate the reflectivity variations for biomass ranging from 80 to 120 t/ha. The tree height is estimated from lidar data.

TABLE 3. SUMMARY OF SENSITIVITY TO SM FROM THE DIFFERENT EXPERIMENTS. INDICATED IN DB PER UNIT OF VOLUMETRIC SOIL MOISTURE (IN m^3/m^3) AND AS DYNAMIC RANGE OVER THE TYPICAL RANGE OF SM (BETWEEN 0 AND 0.4 m^3/m^3).

	EMPIRICAL II = 0–30°	THEORETICAL
TDS-1 (VOD theoretically corrected)	7 dB/1 m^3m^{-3} **3 dB/0.4 m^3m^{-3}**	**6 ÷ 6.8 dB/0.4 m^3m^{-3}**
CyGNSS	15 dB/1 m^3m^{-3} **6 dB/0.4 m^3m^{-3}**	
CyGNSS binned	~18 dB/1 m^3m^{-3} (θ_i ~independent) **~7 dB/0.4 m^3m^{-3}**	
CyGNSS VOD and σ empirically corrected	26 dB/1 m^3m^{-3} (θ_i ~independent) **~10 dB/0.4 m^3m^{-3}**	
GLORI	**~18 ÷ 11 dB/0.4 m^3m^{-3}** (relatively dry case)	

TABLE 4. SUMMARY OF SENSITIVITY OF SPACEBORNE REFLECTIVITY TO DIFFERENT FOREST PARAMETERS DERIVED FROM LOCAL AND GLOBAL SCALE ANALYSIS.

SENSITIVITY TO	LOCAL	GLOBAL	THEORETICAL
VOD (Np)	−16 dB/1 VOD	−7 dB/1 VOD	< −11 dB/1 VOD
AGB (t/ha)	−0.05 dB/tha^{-1} 18 dB/[50–400 t/ha]	−0.01 dB/tha^{-1}	26 dB/[50–400 t/ha]
Tree height (m)	−0.7 dB/m	−0.23 dB/m	

the signal was expected to be prevalently coherent as in the case of flat surfaces [16].

In conclusion, many sources of signal fluctuation were observed caused by nonsystematic sampling over time of an inhomogeneous Earth's surface, the influence of nuisance parameters (such as topography), and speckle effects not mitigated by the incoherent integration. Other sources of uncertainty are likely related to calibration issues (e.g., unknown changes in the transmitted power, antenna gain characterization, and so on) that are not completely solved in the current missions. Those fluctuations must be mitigated to achieve reasonable retrieval performances of the target quantities. Thus, a proper strategy for calibration, noise mitigation, and spatial and temporal aggregation has to be carried out, leading to final resolutions of the products still to be optimized.

The retrieval exercises carried out during the project indicate contradictory retrieval results, depending on the space–time averaging. In particular, the comparison of single-shot retrievals (i.e., not averaged in time) with reference data was always very poor, and the removal of unwanted physical quantities affecting the signal was not effective (e.g., mitigation of the vegetation and roughness effects to retrieve the SM). It was very difficult to combine single-shot GNSS reflectivity with the right ancillary parameters (e.g., roughness and VOD) to derive the SM, even if the former were accurately measured. The highly fluctuating behavior of the signal can explain this outcome.

However, for averaged quantities, such as biomass maps derived over a long time frame or daily SM maps, the retrieval performances were promising. Simple empirical linear regressions suffered from the nonlinear dependence of reflectivity from surface parameters, whereas change detection techniques, although capable of coping with local effects (assuming they can be considered stationary), do not provide absolute quantities (but only a temporal change of the target parameter). Machine learning techniques can overcome those problems, although the consideration of the physical mechanisms affecting the signal should be carefully taken into account, especially to mitigate the risk of overfitting with a blind use of input data. For SM retrieval, an issue was identified in the case of very dry soil, likely associated to deeper penetration into a stratified terrain. The selection of required ancillary information in the retrieval algorithms should be further improved as well as the combination with other satellite data (e.g., monostatic radar or microwave radiometers).

Based on the previous considerations, three objectives are considered a priority for further research in this field. First, the capability to predict the signal over land by the simulators should be confirmed, considering data from the CyGNSS constellation and of the future HydroGNSS mission, and also comparing the absolute calibration and model validation based on *TDS-1* data. Second, the fluctuating behavior of the signal should be better understood. Finally, the use of more sophisticated retrieval techniques based on neural networks should be further expanded to appreciate the real performances of GNSS-R with respect to well-established and consolidated products from other Earth observation techniques (e.g., microwave radiometers). Future data sets and future missions with enhanced features will help improve the potential and the quality of the retrieval of biogeophysical parameters, especially the biomass variable and the freeze–thaw state, which are relatively more immature and demand more accurate investigations.

ACKNOWLEDGMENTS

This study has been conducted in the framework of the ESA contract 4000120299/17/NL/AF/hh, "Potential of Spaceborne GNSS-R for Land Applications." The *TDS-1* data have been freely collected from the MERRBYS portal at merrbys.co.uk. The CyGNSS and SMAP data were downloaded from the NASA Earthdata portal at podaac.jpl.nasa.gov and nsidc.org/data/smap, respectively. The SMOS data are made available from the ESA through the smos-diss.eo.esa.int website. This work has also been partially supported by the project of the Ministerio de Ciencia, Innovación y Universidades and EU ERDF ref. RTI2018-099008-B-C21/AEI/10.13089/E01100011083, "Sensing with Pioneering Opportunistic Techniques," and grant MDM-2016-0600 to the CommSensLab-UPC "María de Maeztu" Excellent Research Unit. We thank the ISMN for the availability of soil moisture data.

AUTHOR INFORMATION

Nazzareno Pierdicca (nazzareno.pierdicca@uniroma1.it) is with "Sapienza" University, Rome, 00184, Italy.

Davide Comite (davide.comite@uniroma1.it) is with "Sapienza" University, Rome, 00184, Italy.

Adriano Camps (adriano.jose.camps@upc.edu) is with Universitat Politècnica de Catalunya, Barcelona, 08034, Spain.

Hugo Carreno-Luengo (carreno@umich.edu) is with the University of Michigan, Ann Arbor, Michigan, 48109-1382, USA.

Luca Cenci (luca.cenci@serco.com) is with Serco Italia SpA, Frascati, 00044, Italy.

Maria Paola Clarizia (maria-paola.clarizia@deimos-space.com) is with Deimos Space UK, Didcot, OX11 0QR, UK.

Fabiano Costantini (fabiano.costantini@deimos-space.com) is with DEIMOS Engenharia S.A., Harwell, UK.

Laura Dente (laura.dente@uniroma2.it) is with the University of Rome Tor Vergata, Rome, 00133, Italy.

Leila Guerriero (leila.guerriero@uniroma2.it) is with the University of Rome Tor Vergata, Rome, 00133, Italy.

Antonio Mollfulleda (antonio.mollfulleda@starlab-int.com) is with Starlab UK Ltd., Barcelona, 08035, Spain.

Simonetta Paloscia (s.paloscia@ifac.cnr.it) is with the National Research Council, IFAC Institute, Florence, 50127, Italy.

Hyuk Park (park.hyuk@upc.edu) is with Universitat Politècnica de Catalunya, Barcelona, 08034, Spain.

Emanuele Santi (e.santi@ifac.cnr.it) is with the National Research Council, IFAC Institute, Florence, 50127, Italy.

Mehrez Zribi (mehrez.zribi@ird.fr) is with Université Toulouse III Paul Sabatier, Toulouse, 31400, France.

Nicolas Floury (nicolas.floury@esa.int) is with the European Space Agency/European Space Research and Technology Centre, Noordwijk, NL-2200AG, The Netherlands.

REFERENCES

[1] M. Martin-Neira, "A passive reflectometry and interferometry system (PARIS): Application to ocean altimetry," *ESA J.*, vol. 17, no. 4, pp. 331–355, 1993.

[2] J. L. Garrison and S. J. Katzberg, "The application of reflected GPS signals to ocean remote sensing," *Remote Sens. Environ.*, vol. 73, no. 2, pp. 175–187, 2000. doi: 10.1016/S0034-4257(00)00092-4.

[3] V. U. Zavorotny, S. Gleason, E. Cardellach, and A. Camps, "Tutorial on remote sensing using GNSS bistatic radar of opportunity," *IEEE Geosci. Remote Sens. Mag.*, vol. 2, no. 4, pp. 8–45, 2014. doi: 10.1109/MGRS.2014.2374220.

[4] C. S. Ruf et al., "A new paradigm in earth environmental monitoring with the CyGNSS small satellite constellation," *Sci. Rep.*, vol. 8, no. 11, p. 8782, June 2018. doi: 10.1038/s41598-018-27127-4.

[5] M. Martin-Neira, S. D'Addio, C. Buck, N. Floury, and R. Prieto-Cerdeira, "The PARIS ocean altimeter in-orbit demonstrator," *IEEE Trans. Geosci. Remote Sens.*, vol. 49, no. 6, pp. 2209–2237, June 2011. doi: 10.1109/TGRS.2010.2092431.

[6] A. Camps et al., "Optimization and performance analysis of interferometric GNSS-R altimeters: Application to the PARIS IoD mission," *IEEE J. Sel. Topics Appl. Earth Observ. Remote Sens.*, vol. 7, no. 5, pp. 1436–1451, May 2014. doi: 10.1109/JSTARS.2014.2320873.

[7] J. Wickert et al., "GEROS-ISS: GNSS reflectometry, radio occultation, and scatterometry onboard the International Space Station," *IEEE J. Sel. Topics Appl. Earth Observ. Remote Sens.*, vol. 9, no. 10, pp. 4552–4581, Oct. 2016. doi: 10.1109/JSTARS.2016.2614428.

[8] E. Cardellach et al., "GNSS transpolar Earth reflectometry exploring system (G-TERN): Mission concept," *IEEE Access*, vol. 6, pp. 13,980–14,018, Mar. 2018. doi: 10.1109/ACCESS.2018.2814072.

[9] M. Unwin et al., "An Introduction to the HydroGNSS GNSS reflectometry remote sensing mission," *IEEE J. Sel. Topics Appl. Earth Observ. Remote Sens.*, vol. 14, pp. 6987–6999, June 2021. doi: 10.1109/JSTARS.2021.3089550.

[10] H. Carreno-Luengo, G. Luzi, and M. Crosetto, "Sensitivity of CyGNSS bistatic reflectivity and SMAP microwave radiometry brightness temperature to geophysical parameters over land surfaces," *IEEE J. Sel. Topics Appl. Earth Observ. Remote Sens.*, vol. 12, no. 1, pp. 107–122, 2019. doi: 10.1109/JSTARS.2018.2856588.

[11] A. Camps, A. Alonso-Arroyo, H. Park, R. Onrubia, D. Pascual, and J. Querol, "L-band vegetation optical depth estimation using transmitted GNSS signals: Application to GNSS-reflectometry and positioning," *Remote Sens.*, vol. 12, no. 15, p. 2352, 2020. doi: 10.3390/rs12152352.

[12] E. Motte et al., "GLORI: A GNSS-R dual polarization airborne instrument for land surface monitoring," *Sensors*, vol. 16, no. 5, p. 732, 2016. doi: 10.3390/s16050732.

[13] A. Egido et al., "Global navigation satellite systems reflectometry as a remote sensing tool for agriculture," *Remote Sens.*, vol. 4, no. 8, pp. 2356–2372, 2012. doi: 10.3390/rs4082356.

[14] P. Ferrazzoli, L. Guerriero, N. Pierdicca, and R. Rahmoune, "Forest biomass monitoring with GNSS-R: Theoretical simulations," *Adv. Space Res.*, vol. 47, no. 10, pp. 1823–1832, 2011. doi: 10.1016/j.asr.2010.04.025.

[15] A. Egido et al., "Airborne GNSS-R polarimetric measurements for soil moisture and above-ground biomass estimation," *IEEE J. Sel. Topics Appl. Earth Observ. Remote Sens.*, vol. 7, no. 5, pp. 1522–1532, 2014. doi: 10.1109/JSTARS.2014.2322854.

[16] D. Comite and N. Pierdicca, "Decorrelation of the near-specular land scattering in bistatic radar systems," *IEEE Trans. Geosci. Remote Sens.*, early access, 2020. doi: 10.1109/TGRS.2021.3072864.

[17] M. Zribi et al., "Potential applications of GNSS-R observations over agricultural areas: Results from the GLORI airborne campaign," *Remote Sens.*, vol. 10, no. 8, p. 1245, 2018. doi: 10.3390/rs10081245.

[18] R. Onrubia et al., "Preliminary altimetry results of the MALYGNSS instrument in the HUMIT project," in *Proc. IEEE Int. Geosci. Remote Sens. Symp.*, 2018, pp. 3331–3334. doi: 10.1109/IGARSS.2018.8518636.

[19] A. Camps, M. Vall-llossera, H. Park, G. Portal, and L. Rossato, "Sensitivity of TDS-1 GNSS-R reflectivity to soil moisture: Global and regional differences and impact of different spatial scales," *Remote Sens.*, vol. 10, no. 11, pp. 1856-1–1856-19, Nov. 2018. doi: 10.3390/rs10111856.

[20] N. Rodriguez-Alvarez, E. Podest, K. Jensen, and K. C. McDonald, "Classifying inundation in a tropical wetlands complex with GNSS-R," *Remote Sens.*, vol. 11, no. 9, p. 1053, 2019. doi: 10.3390/rs11091053.

[21] K. Jensen, K. McDonald, E. Podest, N. Rodriguez-Alvarez, V. Horna, and N. Steiner, "Assessing L-band GNSS-reflectometry and imaging radar for detecting sub-canopy inundation dynamics in a tropical wetlands complex," *Remote Sens.*, vol. 10, no. 9, p. 1431, 2018. doi: 10.3390/rs10091431.

[22] C. Chew, J. T. Reager, and E. Small, "CYGNSS data map flood inundation during the 2017 Atlantic hurricane season," *Sci. Rep.*, vol. 8, no. 1, pp. 1–8, 2018. doi: 10.1038/s41598-018-27673-x.

[23] T. Beltramonte, M. di Bisceglie, C. Galdi, and I. M. Russo, "Remote sensing of inland waters with signals of opportunity from global navigation satellite systems," in *Proc. IEEE Int. Forum Res. Technol. Soc. Ind. (RTSI)*, 2019, pp. 115–119. doi: 10.1109/RTSI.2019.8895573.

[24] S. V. Nghiem et al., "Wetland monitoring with global navigation satellite system reflectometry," *Earth Space Sci.*, vol. 4, no. 1, pp. 16–39, 2017. doi: 10.1002/2016EA000194.

[25] W. Li, E. Cardellach, F. Fabra, S. Ribó, and A. Rius, "Measuring Greenland ice sheet melt using spaceborne GNSS reflectometry from TechDemoSat-1," *Geophys. Res. Lett.*, vol. 47, no. 2, p. e2019GL086477, 2020. doi: 10.1029/2019GL086477.

[26] Y. Wang and Y. J. Morton, "Coherent GNSS reflection signal processing for high-precision and high-resolution spaceborne applications," *IEEE Trans. Geosci. Remote Sens.*, vol. 59, no. 1, pp. 831–842, 2020. doi: 10.1109/TGRS.2020.2993804.

[27] M. Unwin, P. Jales, J. Tye, C. Gommenginger, G. Foti, and J. Rosello, "Spaceborne GNSS-reflectometry on TechDemoSat-1:

Early mission operations and exploitation," *IEEE J. Sel. Topics Appl. Earth Observ. Remote Sens.*, vol. 9, no. 10, pp. 4525–4539, Sept. 2016. doi: 10.1109/JSTARS.2016.2603846.

[28] D. Comite, L. Cenci, A. Colliander, and N. Pierdicca, "Monitoring freeze-thaw state by means of GNSS reflectometry: An analysis of TechDemoSat-1 data," *IEEE J. Sel. Topics Appl. Earth Observ. Remote Sens.*, vol. 13, pp. 2996–3005, May. 2020. doi: 10.1109/JSTARS.2020.2986859.

[29] X. Wu and J. Shuanggen, "Can we monitor the bare soil freeze-thaw process using GNSS-R? A simulation study," in *Proc. SPIE Earth Observing Missions Sens., Develop., Implementation, Characterization III, Int. Soc. Opt. Photon.*, 2014, vol. 9264, p. 92640I. doi: 10.1117/12.2068776.

[30] X. Wu et al., "First measurement of soil freeze/thaw cycles in the Tibetan plateau using CYGNSS GNSS-R data," *Remote Sens.*, vol. 12, no. 15, p. 2361, 2020. doi: 10.3390/rs12152361.

[31] N. Rodriguez-Alvarez and E. Podest, "Characterization of the land surface freeze/thaw state with SMAP-reflectometry (SMAP-R)," in *Proc. IEEE Int. Geosci. Remote Sens. Symp.*, 2019, pp. 4024–4027. doi: 10.1109/IGARSS.2019.8900166.

[32] C. Chew et al., "SMAP radar receiver measures land surface freeze/thaw state through capture of forward-scattered L-band signals," *Remote Sens. Environ.*, vol. 198, pp. 333–344, Sept. 2017. doi: 10.1016/j.rse.2017.06.020.

[33] Q. Yan, W. Huang, S. Jin, and Y. Jia, "Pan-tropical soil moisture mapping based on a three-layer model from CYGNSS GNSS-R data," *Remote Sens. Environ.*, vol. 247, p. 111,944, Sept. 2020. doi: 10.1016/j.rse.2020.111944.

[34] A. Camps et al., "Sensitivity of GNSS-R spaceborne observations to soil moisture and vegetation," *IEEE J. Sel. Topics Appl. Earth Observ. Remote Sens.*, vol. 9, no. 10, pp. 4730–4742, Oct. 2016. doi: 10.1109/JSTARS.2016.2588467.

[35] C. Chew and E. Small, "Soil moisture sensing using spaceborne GNSS reflections: Comparison of CyGNSS reflectivity to SMAP soil moisture," *Geophys. Res. Lett.*, vol. 45, no. 9, pp. 4049–4057, Apr. 2018. doi: 10.1029/2018GL077905.

[36] E. Santi et al., "Remote sensing of forest biomass using GNSS reflectometry," *IEEE J. Sel. Topics Appl. Earth Observ. Remote Sens.*, vol. 13, pp. 2351–2368, May 2020. doi: 10.1109/JSTARS.2020.2982993.

[37] H. Carreno-Luengo, G. Luzi, and M. Crosetto, "Above-ground biomass retrieval over tropical forests: A novel GNSS-R approach with CyGNSS," *Remote Sens.*, vol. 12, no. 9, p. 1368, 2020. doi: 10.3390/rs12091368.

[38] L. Guerriero et al., "Ground-based remote sensing of forests exploiting GNSS signals," *IEEE Trans. Geosci. Remote Sens.*, vol. 58, no. 10, pp. 6844–6860, 2020. doi: 10.1109/TGRS.2020.2976899.

[39] J. F. Munoz-Martin et al., "In-orbit validation of the FMPL-2 instrument—The GNSS-R and L-Band microwave radiometer payload of the FSSCat mission," *Remote Sens.*, vol. 13, no. 1, p. 121, 2021. doi: 10.3390/rs13010121.

[40] C. Chew, R. Shah, C. Zuffada, G. Hajj, D. Masters, and A. J. Mannucci, "Demonstrating soil moisture remote sensing with observations from the UK TechDemoSat-1 satellite mission," *Geophys. Res. Lett.*, vol. 43, no. 7, pp. 3317–3324, 2016. doi: 10.1002/2016GL068189.

[41] C. Chew and E. Small, "Description of the UCAR/CU soil moisture product," *Remote Sens.*, vol. 12, no. 10, p. 1558, 2020. doi: 10.3390/rs12101558.

[42] V. Senyurek, F. Lei, D. Boyd, A. C. Gurbuz, M. Kurum, and R. Moorhead, "Evaluations of machine learning-based CYGNSS soil moisture estimates against SMAP observations," *Remote Sens.*, vol. 12, no. 21, p. 3503, 2020. doi: 10.3390/rs12213503.

[43] O. Eroglu, M. Kurum, D. Boyd, and A. C. Gurbuz, "High spatio-temporal resolution CYGNSS soil moisture estimates using artificial neural networks," *Remote Sens.*, vol. 11, no. 19, p. 2272, 2019. doi: 10.3390/rs11192272.

[44] S. H. Yueh et al., "A semiempirical modeling of soil moisture, vegetation, and surface roughness impact on CYGNSS reflectometry data," *IEEE Trans. Geosci. Remote Sens.*, early access, 2021. doi: 10.1109/TGRS.2020.3035989.

[45] M. M. Al-Khaldi, J. T. Johnson, A. J. O'Brien, A. Balenzano, and F. Mattia, "Time-series retrieval of soil moisture using CYGNSS," *IEEE Trans. Geosci. Remote Sens.*, vol. 57, no. 7, pp. 4322–4331, July 2019. doi: 10.1109/TGRS.2018.2890646.

[46] H. Carreno-Luengo, S. Lowe, C. Zuffada, S. Esterhuizen, and S. Oveisgharan, "Spaceborne GNSS-R from the SMAP mission: First assessment of polarimetric scatterometry over land and cryosphere," *Remote Sens.*, vol. 9, no. 4, p. 362, 2017. doi: 10.3390/rs9040362.

[47] E. Santi et al., "Soil moisture and forest biomass retrieval on a global scale by using CyGNSS data and artificial neural networks," in *Proc. IEEE Int. Geosci. Remote Sens. Symp.*, 2020, pp. 5905–5908. doi: 10.1109/IGARSS39084.2020.9323896.

[48] H. Park et al., "A generic level 1 simulator for spaceborne GNSS-R missions and application to GEROS-ISS ocean reflectometry," *IEEE J. Sel. Topics Appl. Earth Observ. Remote Sens.*, vol. 10, no. 10, pp. 4645–4659, 2017. doi: 10.1109/JSTARS.2017.2720625.

[49] H. Park, A. Camps, J. Castellvi, and J. Muro, "Generic performance simulator of spaceborne GNSS-reflectometer for land applications," *IEEE J. Sel. Topics Appl. Earth Observ. Remote Sens.*, vol. 13, pp. 3179–3191, June 2020. doi: 10.1109/JSTARS.2020.3000391.

[50] N. Pierdicca, L. Guerriero, R. Giusto, M. Brogioni, and A. Egido, "SAVERS: A simulator of GNSS reflections from bare and vegetated soils," *IEEE Trans. Geosci. Remote Sens.*, vol. 52, no. 10, pp. 6542–6554, 2014. doi: 10.1109/TGRS.2013.2297572.

[51] L. Dente, L. Guerriero, D. Comite, and N. Pierdicca, "Spaceborne GNSS-R signal over a complex topography: Modelling and validation," *IEEE J. Sel. Topics Appl. Earth Observ. Remote Sens.*, vol. 13, pp. 1218–1233, Mar. 2020. doi: 10.1109/JSTARS.2020.2975187.

[52] D. Comite, F. Ticconi, L. Dente, L. Guerriero, and N. Pierdicca, "Bistatic coherent scattering from rough soils with application to GNSS reflectometry," *IEEE Trans. Geosci. Remote Sens.*, vol. 58, no. 1, pp. 612–625, 2020. doi: 10.1109/TGRS.2019.2938442.

[53] N. Pierdicca et al., "Potential of spaceborne GNSS-R for land applications," European Space Agency, Paris, France, Final Rep. ESA/ESTEC CONTRACT n. 4000120299/17/NL/AF/hh, GLAFR/1.2019, Sept. 30, 2019.

[54] "Measurement of earth reflected radio-navigation signals by satellite," MERRByS. http://merrbys.org

[55] C. Ruf et al., *CYGNSS Handbook*, 1st ed. Ann Arbor, MI: Michigan Publishing, Apr. 1, 2016, p. 154.

[56] "Physical oceanography distributed active archive center," NASA, Washington, D.C. [Online]. Available: https://podaac.jpl.nasa.gov/

[57] F. Ulaby and D. Long, *Microwave Radar and Radiometric Remote Sensing*. Norwood, MA: Artech House, 2015.

[58] N. Pierdicca et al., "Spaceborne GNSS reflectometry data for land applications: An analysis of Techdemosat data," in *Proc. IEEE Int. Geosci. Remote Sens. Symp.*, 2018, pp. 3351–3354. doi: 10.1109/IGARSS.2018.8517987.

[59] A. M. Balakhder, M. M. Al-Khaldi, and J. T. Johnson, "On the coherency of ocean and land surface specular scattering for GNSS-R and signals of opportunity systems," *IEEE Trans. Geosci. Remote Sens.*, vol. 57, no. 12, pp. 10,426–10,436, Dec. 2019. doi: 10.1109/TGRS.2019.2935257.

[60] H. Xu, J. Zhu, L. Tsang, and S. B. Kim, "A fine scale partially coherent patch model including topographical effects for GNSS-R DDM simulations," *Progr. Electromagn. Res.*, vol. 170, pp. 97–128, Feb. 2021. doi: 10.2528/PIER20121201.

[61] M. Simard, N. Pinto, J. B. Fisher, and A. Baccini, "Mapping forest canopy height globally with spaceborne lidar," *J. Geophys. Res.*, vol. 116, p. G04021, 2011. doi: 10.1029/2011JG001708.

[62] V. Avitabile et al., "An integrated pan-tropical biomass maps using multiple reference datasets," *Global Change Biol.*, vol. 22, no. 4, pp. 1406–1420. doi: 10.1111/gcb.13139.

[63] P. A. Burek, J. M. Van Der Knijff, and A. De Roo, "LISFLOOD – Distributed water balance and flood simulation model – Revised user manual," Publications Office of the European Union, Luxembourg, Tech. Rep. EUR 26162 EN, 2013.

[64] A. Camps, H. Park, J. Castellví, J. Corbera, and E. Ascaso, "Single-pass soil moisture retrievals using GNSS-R: Lessons learned," *Remote Sens.*, vol. 12, no. 12, p. 2064, 2020. doi: 10.3390/rs12122064.

[65] J. C. Jenkins, D. C. Chojnacky, L. S. Heath, and R. A. Birdsey, "National scale biomass estimators for United States tree species," *Forest Sci.*, vol. 49, pp. 12–35, Feb. 2003.

[66] A. Camps and J. F. Munoz-Martin, "Analytical computation of the spatial resolution in GNSS-R and experimental validation at L1 and L5," *Remote Sens.*, vol. 12, no. 23, p. 3910, 2020. doi: 10.3390/rs12233910.

[67] H. Carreno-Luengo, C. Ruf, A. Warnock, and K. Brunner, "Investigating the impact of coherent and incoherent scattering terms in GNSS-R delay doppler maps," in *Proc. IEEE Int. Geosci. Remote Sens. Symp.*, Hawaii, early access, July 2020. doi: 10.1109/IGARSS39084.2020.9324404.

[68] A. Camps, "Spatial resolution in GNSS-R under coherent scattering," *IEEE Geosci. Remote Sens. Lett.*, vol. 17, no. 1, pp. 32–36, 2020. doi: 10.1109/LGRS.2019.2916164.

[69] G. Portal et al., "A spatially consistent downscaling approach for SMOS using an adaptive moving window," *IEEE J. Sel. Topics Appl. Earth Observ. Remote Sens.*, vol. 11, no. 6, pp. 1883–1894, May 2018. doi: 10.1109/JSTARS.2018.2832447.

[70] M. Piles et al., "A downscaling approach for SMOS land observations: Evaluation of high-resolution soil moisture maps over the Iberian Peninsula," *IEEE J. Sel. Topics Appl. Earth Observ. Remote Sens.*, vol. 7, no. 9, pp. 3845–3857, Sept. 2014. doi: 10.1109/JSTARS.2014.2325398.

[71] M. Zribi, M. Foucras, N. Baghdadi, J. Demarty, and S. Muddu, "A new reflectivity index for the retrieval of surface soil moisture from radar data," *IEEE J. Sel. Topics Appl. Earth Observ. Remote Sens.*, vol. 14, pp. 818–826, 2021. doi: 10.1109/JSTARS.2020.3033132.

[72] A. Perez-Portero, J. F. Munoz-Martin, H. Park, and A. Camps, "Airborne GNSS-R: A key enabling technology for environmental monitoring," *IEEE J. Sel. Topics Appl. Earth Observ. Remote Sens.*, vol. 14, pp. 6652–6661, Apr. 2021. doi: 10.1109/JSTARS.2021.3076003.

[73] M. Zribi, M. Huc, T. Pellarin, N. Baghdadi, and N. Pierdicca, "Soil moisture retrieval using GNSS-R data," in *Proc. IEEE Mediterranean Middle-East Geosci. Remote Sens. Symp.*, 2020, pp. 172–175. doi: 10.1109/M2GARSS47143.2020.9105320.

[74] P. O'Neill, R. Bindlish, S. Chan, E. Njoku, and T. Jackson, "Soil moisture active passive (SMAP), algorithm theoretical basis document level 2 & 3 soil moisture (passive) data products, revision D," Jet Propulsion Laboratory, Pasadena, CA, Ref. JPL D-66480, June 6, 2018.

[75] R. Acevo-Herrera et al., "Design and first results of an UAV-borne L-band radiometer for multiple monitoring purposes," *Remote Sens.*, vol. 2, no. 7, pp. 1662–1679, 2010. doi: 10.3390/rs2071662.

[76] J. F. Munoz-Martin et al., "Single-pass soil moisture retrieval using GNSS-R at L1 and L5 bands: Results from airborne experiment," *Remote Sens.*, vol. 13, no. 4, p. 797, 2021. doi: 10.3390/rs13040797.

[77] J. F. Munoz-Martin et al., "Soil moisture estimation synergy using GNSS-R and L-Band microwave radiometry data from FSSCat/FMPL-2," *Remote Sens.*, vol. 13, no. 5, p. 994, 2021. doi: 10.3390/rs13050994.

[78] W. Wagner, G. Lemoine, and H. Rott, "A method for estimating soil moisture from ERS scatterometer and soil data," *Remote Sens. Environ.*, vol. 70, no. 2, pp. 191–207, Nov. 1999. doi: 10.1016/S0034-4257(99)00036-X.

[79] M. P. Clarizia, N. Pierdicca, F. Costantini, and N. Floury, "Analysis of CyGNSS data for soil moisture retrieval," *IEEE J. Sel. Topics Appl. Earth Observ. Remote Sens.*, vol. 12, no. 7, pp. 2227–2235, 2019. doi: 10.1109/JSTARS.2019.2895510.

[80] M. Zribi et al., "Performance of GNSS-R GLORI data for biomass estimation over the Landes forest," *Int. J. Appl. Earth Observ. Geoinf.*, vol. 74, pp. 150–158, Feb. 2019. doi: 10.1016/j.jag.2018.09.010.

[81] E. Santi, S. Paloscia, S. Pettinato, and G. Fontanelli, "Application of artificial neural networks for the soil moisture retrieval from active and passive microwave spaceborne sensors," *Int. J. Appl. Earth Observ. Geoinf.*, vol. 48, pp. 61–73, June 2016. doi: 10.1016/j.jag.2015.08.002.

[82] D. Comite, L. Dente, L. Guerriero, and N. Pierdicca, "Modeling the coherence of scattered signals of opportunity," in *Proc. IEEE Int. Geosci. Remote Sens. Symp.*, 2019, pp. 4819–4822. doi: 10.1109/IGARSS.2019.8897960.

GRS